Eur. Phys. J. C (2017) 77:268
DOI 10.1140/epjc/s10052-017-4810-0

THE EUROPEAN PHYSICAL JOURNAL C

Regular Article - Theoretical Physics

Likelihood analysis of the minimal AMSB model

E. Bagnaschi[1], M. Borsato[2,a], K. Sakurai[3,4], O. Buchmueller[5], R. Cavanaugh[6,7], V. Chobanova[2], M. Citron[5], J. C. Costa[5], A. De Roeck[8,9], M. J. Dolan[10], J. R. Ellis[11,12], H. Flächer[13], S. Heinemeyer[14,15,16], G. Isidori[17], M. Lucio[2], F. Luo[18], D. Martínez Santos[2], K. A. Olive[19], A. Richards[5], G. Weiglein[1]

[1] DESY, Notkestraße 85, 22607 Hamburg, Germany
[2] Universidade de Santiago de Compostela, 15706 Santiago de Compostela, Spain
[3] Science Laboratories, Department of Physics, Institute for Particle Physics Phenomenology, University of Durham, South Road, Durham DH1 3LE, UK
[4] Faculty of Physics, Institute of Theoretical Physics, University of Warsaw, ul. Pasteura 5, 02-093 Warsaw, Poland
[5] High Energy Physics Group, Blackett Laboratory, Imperial College, Prince Consort Road, London SW7 2AZ, UK
[6] Fermi National Accelerator Laboratory, P.O. Box 500, Batavia, IL 60510, USA
[7] Physics Department, University of Illinois at Chicago, Chicago, IL 60607-7059, USA
[8] Experimental Physics Department, CERN, 1211 Geneva 23, Switzerland
[9] Antwerp University, 2610 Wilrijk, Belgium
[10] ARC Centre of Excellence for Particle Physics at the Terascale, School of Physics, University of Melbourne, Melbourne 3010, Australia
[11] Theoretical Particle Physics and Cosmology Group, Department of Physics, King's College London, London WC2R 2LS, UK
[12] Theoretical Physics Department, CERN, 1211 Geneva 23, Switzerland
[13] H.H. Wills Physics Laboratory, University of Bristol, Tyndall Avenue, Bristol BS8 1TL, UK
[14] Campus of International Excellence UAM+CSIC, Cantoblanco, 28049 Madrid, Spain
[15] Instituto de Física Teórica UAM-CSIC, C/ Nicolas Cabrera 13-15, 28049 Madrid, Spain
[16] Instituto de Física de Cantabria (CSIC-UC), Avda. de Los Castros s/n, 39005 Cantabria, Spain
[17] Physik-Institut, Universität Zürich, 8057 Zurich, Switzerland
[18] Kavli IPMU (WPI), UTIAS, The University of Tokyo, Kashiwa, Chiba 277-8583, Japan
[19] William I. Fine Theoretical Physics Institute, School of Physics and Astronomy, University of Minnesota, Minneapolis, MN 55455, USA

Received: 21 December 2016 / Accepted: 5 April 2017

Abstract We perform a likelihood analysis of the minimal anomaly-mediated supersymmetry-breaking (mAMSB) model using constraints from cosmology and accelerator experiments. We find that either a wino-like or a Higgsino-like neutralino LSP, $\tilde{\chi}_1^0$, may provide the cold dark matter (DM), both with similar likelihoods. The upper limit on the DM density from Planck and other experiments enforces $m_{\tilde{\chi}_1^0} \lesssim 3$ TeV after the inclusion of Sommerfeld enhancement in its annihilations. If most of the cold DM density is provided by the $\tilde{\chi}_1^0$, the measured value of the Higgs mass favours a limited range of $\tan\beta \sim 5$ (and also for $\tan\beta \sim 45$ if $\mu > 0$) but the scalar mass m_0 is poorly constrained. In the wino-LSP case, $m_{3/2}$ is constrained to about 900 TeV and $m_{\tilde{\chi}_1^0}$ to 2.9 ± 0.1 TeV, whereas in the Higgsino-LSP case $m_{3/2}$ has just a lower limit $\gtrsim 650$ TeV ($\gtrsim 480$ TeV) and $m_{\tilde{\chi}_1^0}$ is constrained to 1.12 (1.13) $\pm$ 0.02 TeV in the $\mu > 0$ ($\mu < 0$) scenario. In neither case can the anomalous magnetic moment of the muon, $(g-2)_\mu$, be improved significantly relative to its Standard Model (SM) value, nor do flavour measurements constrain the model significantly, and there are poor prospects for discovering supersymmetric particles at the LHC, though there are some prospects for direct DM detection. On the other hand, if the $\tilde{\chi}_1^0$ contributes only a fraction of the cold DM density, future LHC $\not{E}_T$-based searches for gluinos, squarks and heavier chargino and neutralino states as well as disappearing track searches in the wino-like LSP region will be relevant, and interference effects enable BR($B_{s,d} \to \mu^+\mu^-$) to agree with the data better than in the SM in the case of wino-like DM with $\mu > 0$.

1 Introduction

In previous papers [1–8] (For more information and updates, please see http://cern.ch/mastercode/.) we have presented likelihood analyses of the parameter spaces of various scenarios for supersymmetry (SUSY) breaking, including the CMSSM [9–25], in which soft SUSY breaking parameters are constrained to be universal at the grand unification scale, models in which Higgs masses are allowed to be non-universal (NUHM1,2) [26–32], a model in which 10 soft

[a] e-mail: martino.borsato@cern.ch

Published online: 27 April 2017

SUSY-breaking parameters were treated as free phenomenological parameters (the pMSSM10) [33–47] and one with SU(5) GUT boundary conditions on soft supersymmetry-breaking parameters [48]. These analyses took into account the strengthening direct constraints from sparticle searches at the LHC, as well as indirect constraints based on electroweak precision observables (EWPOs), flavour observables and the contribution to the density of cold dark matter (CDM) in the Universe from the lightest supersymmetric particle (LSP), assuming that it is a neutralino and that R-parity is conserved [49,50]. In particular, we analysed the prospects within these scenarios for discovering SUSY at the LHC and/or in future direct dark matter searches [7].

In this paper we extend our previous analyses of GUT-based models [1–8] by presenting a likelihood analysis of the parameter space of the minimal scenario for anomaly-mediated SUSY breaking (the mAMSB) [51–69]. The spectrum of this model is quite different from those of the CMSSM, NUHM1 and NUHM2, with a different composition of the LSP. Consequently, different issues arise in the application of the experimental constraints, as we discuss below. In the mAMSB there are 3 relevant continuous parameters, the gravitino mass, $m_{3/2}$, which sets the scale of SUSY breaking, the supposedly universal soft SUSY-breaking scalar mass,[1] m_0, and the ratio of Higgs vacuum expectation values, $\tan\beta$, to which may be added the sign of the Higgsino mixing parameter, μ. The LSP is either a Higgsino-like or a wino-like neutralino $\tilde{\chi}_1^0$. In both cases the $\tilde{\chi}_1^0$ is almost degenerate with its chargino partner, $\tilde{\chi}_1^\pm$. Within this mAMSB framework, it is well known that if one requires that a wino-like $\tilde{\chi}_1^0$ is the dominant source of the CDM density indicated by Planck measurements of the cosmic microwave background radiation, namely $\Omega_{\rm CDM}h^2 = 0.1186 \pm 0.0020$ [73], $m_{\tilde{\chi}_1^0} \simeq 3$ TeV [74–77] after inclusion of Sommerfeld enhancement effects [78]. If instead the CDM density is to be explained by a Higgsino-like $\tilde{\chi}_1^0$, $m_{\tilde{\chi}_1^0}$ takes a value of 1.1 TeV. In both cases, sparticles are probably too heavy to be discovered at the LHC, and supersymmetric contributions to EWPOs, flavour observables and $(g-2)_\mu$ are small.

In the first part of our likelihood analysis of the mAMSB parameter space, we combine the assumption that the LSP is the dominant source of CDM with other measurements, notably of the mass of the Higgs boson, $M_{\rm h} = 125.09 \pm 0.24$ GeV [79] (including the relevant theory uncertainties [80]) and its production and decay rates [81,82]. In addition to solutions in which the $\tilde{\chi}_1^0$ is wino- or Higgsino-like, we also find less-favoured solutions in which the $\tilde{\chi}_1^0$ is a mixed wino–Higgsino state. In the wino case, whereas $m_{3/2}$ and hence $m_{\tilde{\chi}_1^0}$ are relatively well determined, as is the value of $\tan\beta$, the value of m_0 is quite poorly determined, and there is little difference between the values of the global likelihood functions for the two signs of μ. On the other hand, in the case of a Higgsino-like $\tilde{\chi}_1^0$, while $\tan\beta$ has values around 5, m_0 and $m_{3/2}$ are only constrained to be larger than 20 TeV and 600 TeV, respectively, in the positive μ case. For negative μ, the m_0 and $m_{3/2}$ constraints are lowered to 18 TeV and 500 TeV, respectively.

If there is some other contribution to the CDM, so that $\Omega_{\tilde{\chi}_1^0} < \Omega_{\rm CDM}$, the SUSY-breaking mass scale $m_{3/2}$ can be reduced, and hence also $m_{\tilde{\chi}_1^0}$, although the value of $M_{\rm h}$ still imposes a significant lower limit. In this case, some direct searches for sparticles at the LHC also become relevant, notably $\not{E}_T$-based searches for gluinos, squarks and heavier chargino and neutralino states as well as disappearing track searches for the next-to-LSP charged wino. We discuss the prospects for sparticle searches at the LHC in this case and at the 100 TeV FCC-hh collider, and also find that some deviations from Standard Model (SM) predictions for flavour observables may become important, notably ${\rm BR}(b \to s\gamma)$ and ${\rm BR}(B_{s,d} \to \mu^+\mu^-)$.

Using the minimum value of the χ^2 likelihood function and the number of effective degrees of freedom (excluding the constraint from `HiggsSignals` [81,82], as was done in [4–6]) leads to an estimate of ∼11% for the χ^2 probability of the mAMSB model if most of the CDM is due to the $\tilde{\chi}_1^0$, for both signs of μ in both the wino- and Higgsino-like cases. When this CDM condition is relaxed, the χ^2 probability is unchanged if $\mu < 0$, but increases to 18% in the wino-like LSP case if $\mu > 0$ thanks to improved consistency with the experimental measurement of ${\rm BR}(B_{s,d} \to \mu^+\mu^-)$.[2] These χ^2 probabilities for the mAMSB model cannot be compared directly with those found previously for the CMSSM [4], the NUHM1 [4], the NUHM2 [5] and the pMSSM10 [6], since those models were studied with a different dataset that included an older set of LHC data.

The outline of this paper is as follows. In Sect. 2 we review briefly the specification of the mAMSB model. In Sect. 3 we review our implementations of the relevant theoretical, phenomenological, experimental, astrophysical and cosmological constraints, including those from the flavour and Higgs sectors, and from LHC and dark matter searches (see [6,8] for details of our other LHC search implementations). In the case of dark matter we describe in detail our implementation of Sommerfeld enhancement in the calculation of the relic CDM density. Section 4 reviews the `MasterCode` framework.

[1] In pure gravity-mediated models [70–72], m_0 is constrained to be equal to the gravitino mass, resulting in a two-parameter model in which $\tan\beta$ is strongly constrained to a value near 2.

[2] These estimates of the χ^2 probabilities are calculated taking into account the relevant numbers of degrees of freedom using the standard prescription [82]: see Tables 2 and 5, respectively.

Section 5 then presents our results, first under the assumption that the lightest neutralino $\tilde{\chi}_1^0$ is the dominant form of CDM, and then in the more general case when other forms of CDM may dominate. This Section is concluded by the presentation and discussion of the χ^2 likelihood functions for observables of interest. Finally, we present our conclusions in Sect. 6.

2 Specification of the mAMSB model

In AMSB, SUSY breaking arises via a loop-induced super-Weyl anomaly [51–56]. Since the gaugino masses $M_{1,2,3}$ are suppressed by loop factors relative to the gravitino mass, $m_{3/2}$, the latter is fairly heavy in this scenario ($m_{3/2} \gtrsim 20$ TeV) and the wino-like states are lighter than the bino-like ones, with the following ratios of gaugino masses at NLO: $|M_1| : |M_2| : |M_3| \approx 2.8 : 1 : 7.1$. Pure AMSB is, however, an unrealistic model, because renormalization leads to negative squared masses for sleptons and, in order to avoid tachyonic sleptons, the minimal AMSB scenario (mAMSB) adds a constant m_0^2 to all squared scalar masses [57–69]. Thus the mAMSB model has three continuous free parameters: $m_{3/2}$, m_0 and the ratio of Higgs vevs, $\tan\beta$. In addition, the sign of the Higgsino mixing parameter, μ, is also free. The trilinear soft SUSY-breaking mass terms, A_i, are determined by anomalies, like the gaugino masses, and are thus proportional to $m_{3/2}$. The μ term and the Higgs bilinear, B, are determined phenomenologically via the minimization of the Higgs potential, as in the CMSSM.

The following are some characteristic features of mAMSB: near mass-degeneracy of the left and right sleptons: $m_{\tilde{l}_R} \approx m_{\tilde{l}_L}$, and of the lightest chargino and neutralino, $m_{\tilde{\chi}_1^\pm} \approx m_{\tilde{\chi}_1^0}$. The mass hierarchy between sleptons and gauginos is dependent on the numerical values of the input parameters, and the squark masses are typically very heavy, because they contain a term proportional to $g_3^4 m_{3/2}^2$. In addition, the measured Higgs mass and the relatively low values of the trilinears A_i together imply that the stop masses must also be relatively high. The LSP composition may be wino-, Higgsino-like or mixed, as we discuss in more detail below.

3 Implementations of constraints

Our treatments in this paper of many of the relevant constraints follow very closely the implementations in our previous analyses which were recently summarized in [8]. In the following subsections we review the implementations, highlighting new constraints and instances where we implement constraints differently from our previous work.

3.1 Flavour, electroweak and higgs constraints

Constraints from B-physics and K-physics observables are the same as in [8].[3] In particular, we include the recent ATLAS result in our global combination of measurements of $\mathrm{BR}(B_{s,d} \to \mu^+\mu^-)$ [84–87]. In contrast to our previous studies [4–8], in this study we do not evaluate independently the constraints from EWPOs, since for SUSY-breaking parameters in the multi-TeV range they are indistinguishable from the Standard Model values within the current experimental uncertainties, as we have checked using `FeynWZ` [88,89]. The only exception is the mass of the W boson, M_W, which is evaluated using `FeynHiggs`.[4] For the other EWPOs we use the theoretical and experimental values given in the review [82]. We use the combination of ATLAS and CMS measurements of the mass of the Higgs boson: $M_\mathrm{h} = 125.09 \pm 0.24$ GeV [79]. We use a beta-version of the `FeynHiggs 2.12.1` code [80,90–94] to evaluate the constraint this imposes on the mAMSB parameter space. It improves on the `FeynHiggs` versions used for previous analyses [4–7] by including two-loop QCD corrections in the evaluation of the $\overline{\mathrm{DR}}$ running top mass and an improved evaluation of the top mass in the $\overline{\mathrm{DR}}$-on-shell conversion for the scalar tops. At low values of $m_{\tilde{t}_1}$, we use, as previously, a one-σ theoretical uncertainty of 1.5 GeV. In view of the larger theoretical uncertainty at large input parameter values, this uncertainty is smoothly inflated up to 3.0 GeV at $m_{\tilde{t}_1} > 7.5$ TeV, as a conservative estimate. The χ^2 contributions of 85 Higgs search channels from LHC and Tevatron are evaluated using `HiggsSignals` [81,82] and `HiggsBounds` [95–98] as detailed in our previous paper [8].

3.2 LHC constraints

If the entire CDM relic density is provided by the lightest neutralino, all sparticles are heavy, and the current results of the direct sparticle searches at the LHC have no impact on our global fit, though there is some impact from H/A searches [99,100]. On the other hand, if $\tilde{\chi}_1^0$ accounts only for a fraction of the relic CDM density, some sparticles can be light enough to be produced at the LHC. However, as we discuss in more detail later, even for this case we find that the sleptons, the first two generations of squarks and the third-generation squarks are heavier than 0.7, 3.5 and 2.5 TeV at the 2σ level, respectively, well beyond the current LHC sensitivities [101–103]. On the other hand, gluinos and winos

[3] For a previous study of the impact of flavour constraints on the mAMSB model, see [83].

[4] We imposed SU(2) symmetry on the soft SUSY-breaking terms in the $\overline{\mathrm{DR}}$-on-shell conversion of the parameters in the scalar top/bottom sector, leading to a small shift in the values of the scalar bottom masses.

can be as light as 2.5 and 0.5 TeV, respectively, at the 2σ level, so we have considered in more detail the constraints from searches at the LHC. Currently they do not impact the 68 and 95% CL ranges we find for the mAMSB, but some impact can be expected for future LHC runs, as we discuss in Sect. 5.4.

3.3 Dark matter constraints

3.3.1 Sommerfeld enhancement in the wino dark matter region

For a wino-like dark matter particle, the non-perturbative Sommerfeld effect [78] needs to be taken into account in the calculation of the thermal relic abundance. Dedicated studies have been performed in the literature [74–77], with the result that the correct relic abundance is obtained for $m_{\tilde{\chi}_1^0} \simeq 3.1$ TeV (with a spread in numerical results of a few %, which may be taken as an estimate of the uncertainty) after inclusion of Sommerfeld enhancement in the thermally averaged coannihilation cross sections, compared to $m_{\tilde{\chi}_1^0} \simeq 2.3$ TeV at tree level.

Because of the large number of points in our mAMSB sample, we seek a computationally efficient implementation of the Sommerfeld enhancement. We discuss this now, and consider its implications in the following subsections.

It is sufficient for our χ^2 likelihood analysis to use a phenomenological fit for the Sommerfeld enhancement that is applicable near 3.1 TeV. One reason is that, away from ∼3.1 TeV, the χ^2 price rises rapidly due to the very small uncertainty in the Planck result for $\Omega_{\rm CDM}h^2$. Another reason is that the enhancement factor depends very little on the particle spectrum and mostly on $m_{\tilde{\chi}_1^0}$. Therefore, we extract the Sommerfeld factor by using a function to fit the 'non-perturbative' curve in the right panel of Fig. 2 in [74]. One can see that the curve has a dip at ∼2.4 TeV, due to the appearance of a loosely bound state. The calculated relic abundance near the dip is much smaller than the Planck value, so it gives a very large χ^2, and therefore we do not bother to fit the dip. Considering that the Yukawa potential approaches the Coulomb limit for $m_{\tilde{\chi}_1^0} \gg M_{\rm W}$, and that only the electromagnetic force is relevant for $m_{\tilde{\chi}_1^0} \ll M_{\rm W}$, we fit the annihilation cross section using,[5]

$$a_{\rm eff} \equiv a_{\rm eff\,SE=0}\left[\left(c_{\rm pm}S_{\alpha_{\rm em}} + 1 - c_{\rm pm}\right)\left(1-\exp(-\kappa\, M_{\rm W}/m_{\tilde{\chi}_1^0})\right) + S_{\alpha_2}\exp\left(-\kappa\, M_{\rm W}/m_{\tilde{\chi}_1^0}\right)\right], \quad (1)$$

where $a_{\rm eff}$ is the effective s-wave coannihilation cross section (including the Sommerfeld enhancement) for the wino system including the wino-like LSP, $\tilde{\chi}_1^0$, and the corresponding chargino, $\tilde{\chi}_1^\pm$, and $a_{\rm eff\,SE=0}$ is the effective s-wave coannihilation cross section calculated ignoring the enhancement. The latter is defined as

$$a_{\rm eff\,SE=0} \equiv \sum_{i,j} a_{ij} r_i r_j\,, \quad (2)$$

where $r_i \equiv g_i\,(1+\Delta_i)^{3/2}\exp(-\Delta_i m_{\tilde{\chi}_1^0}/T)/g_{\rm eff}$, and $g_{\rm eff} \equiv \sum_k g_k\,(1+\Delta_k)^{3/2}\exp(-\Delta_k m_{\tilde{\chi}_1^0}/T)$ expressed as functions of the temperature, T, at which the coannihilations take place. The indices refer to $\tilde{\chi}_1^0$, $\tilde{\chi}_1^+$ and $\tilde{\chi}_1^-$, and g_i is the number of degrees of freedom, which is 2 for each of the three particles, $\Delta_i \equiv (m_i/m_{\tilde{\chi}_1^0} - 1)$, a_{ij} is the total s-wave (co)annihilation cross section for the processes with incoming particles i and j, and $c_{\rm pm}$ is the fraction of the contribution of the $\tilde{\chi}_1^+\tilde{\chi}_1^-$ s-wave cross section in $a_{\rm eff\,SE=0}$, namely,

$$c_{\rm pm} \equiv \frac{2a_{\tilde{\chi}_1^+\tilde{\chi}_1^-}}{a_{\rm eff\,SE=0}} r_{\tilde{\chi}_1^+} r_{\tilde{\chi}_1^-}. \quad (3)$$

In practice, since $m_{\tilde{\chi}_1^+} - m_{\tilde{\chi}_1^0} \simeq 0.16$ GeV, which is much smaller than the typical temperature of interest in the calculation of the relic abundance for $m_{\tilde{\chi}_1^0}$ near 3.1 TeV, we have $a_{\rm eff\,SE=0} \simeq (a_{\tilde{\chi}_1^0\tilde{\chi}_1^0} + 4a_{\tilde{\chi}_1^0\tilde{\chi}_1^+} + 2a_{\tilde{\chi}_1^+\tilde{\chi}_1^-} + 2a_{\tilde{\chi}_1^+\tilde{\chi}_1^+})/9$, and $c_{\rm pm} \simeq \frac{2}{9}a_{\tilde{\chi}_1^+\tilde{\chi}_1^-}/a_{\rm eff\,SE=0}$. In Eq. (1), $S_{\alpha_{\rm em}}$ and S_{α_2} are the thermally averaged s-wave Sommerfeld enhancement factors for attractive Coulomb potentials with couplings $\alpha_{\rm em}$ and α_2, respectively. We use the function given in Eq. (11) of [104] for these quantities, namely

$$S_{\alpha_x} \equiv \frac{1 + 7y/4 + 3y^2/2 + (3/2-\pi/3)y^3}{1 + 3y/4 + (3/4-\pi/6)y^2}\,, \quad (4)$$

where $y \equiv \alpha_x\sqrt{\pi m_{\tilde{\chi}_1^0}/T}$.

Because the curve in [74] is obtained by taking the massless limit of the SM particles in a_{ij}, we do the same for our fit to obtain the fitting parameter κ. We find that a $\kappa = \mathcal{O}(1)$ can give a good fit for the curve, and that the fit is not sensitive to the exact value of κ. We choose $\kappa = 6$ in our calculation, which gives a good fit around $m_{\tilde{\chi}_1^0} \simeq 3.1$ TeV, in particular.

Equation (1) is used in our calculation of the relic abundance $\Omega_{\tilde{\chi}_1^0}h^2$ for mAMSB models, for which we evaluate $a_{\rm eff\,SE=0}$ and $c_{\rm pm}$ for any parameter point using `SSARD` (Information about this code is available from K. A. Olive: it contains important contributions from J. Evans, T. Falk, A. Ferstl, G. Ganis, F. Luo, A. Mustafayev, J. McDonald, K. A. Olive, P. Sandick, Y. Santoso, V. Spanos, and M. Srednicki.). The perturbative p-wave contribution is also included. We note that, whereas the Sommerfeld enhancement depends almost entirely on $m_{\tilde{\chi}_1^0}$, the values of $a_{\rm eff\,SE=0}$ and $c_{\rm pm}$ depend on the details of the supersymmetric particle spectrum. In particular, due to a cancellation between s- and t-channel contributions in processes with SM fermion anti-fermion pairs in the final states, $a_{\rm eff\,SE=0}$ becomes smaller when the sfermion masses are closer to $m_{\tilde{\chi}_1^0}$.

[5] We emphasize that one can choose a different fitting function, as long as the fit is good near 3.1 TeV.

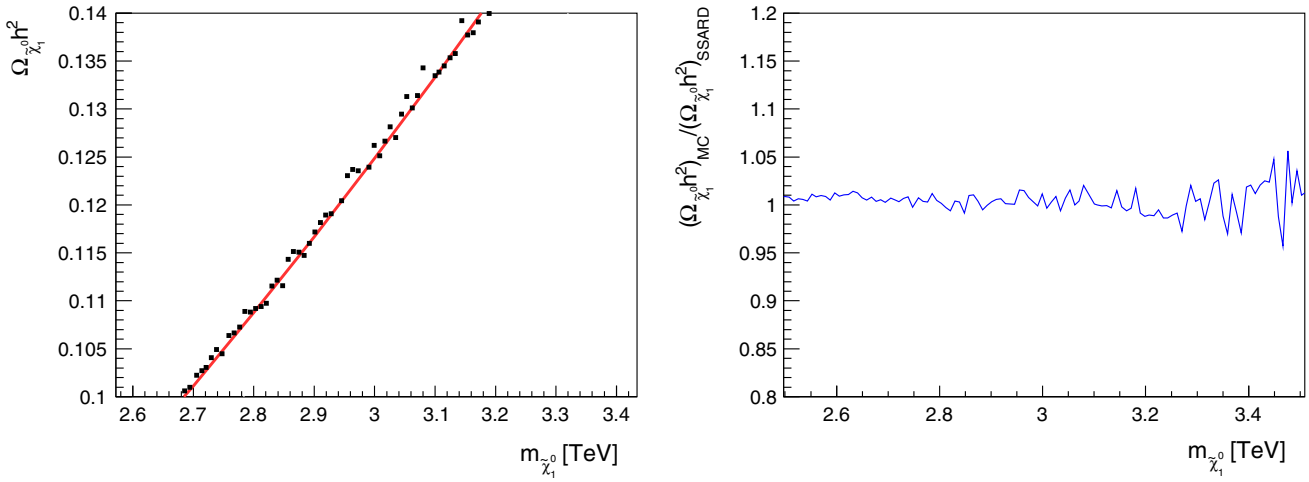

Fig. 1 Calculations of $\Omega_{\tilde{\chi}_1^0}h^2$ comparing results from SSARD and our simplified treatment of the Sommerfeld enhancement in the case of wino dark matter. The *left panel* compares the SSARD calculations (*black dots*) with our Sommerfeld implementation (*red line*), and the *right panel* shows the ratio of the calculated relic densities, connecting the points in the *left panel by a continuous blue line*

For a small subset of our mAMSB parameter sample, we have compared results obtained from our approximate implementation of the Sommerfeld enhancement in the case of wino dark matter with more precise results obtained with SSARD. As seen in the left panel of Fig. 1, our implementation (red line) yields results for the relic density that are very similar to those of complete calculations (black dots). In the right panel we plot the ratio of the relic density calculated using our simplified Sommerfeld implementation for the subsample of mAMSB points to SSARD results, connecting the points at different $m_{\tilde{\chi}_1^0}$ by a continuous blue line. We see that our Sommerfeld implementation agrees with the exact results at the $\lesssim$2% level (in particular when $m_{\tilde{\chi}_1^0} \sim 3$ TeV), an accuracy that is comparable to the current experimental uncertainty from the Planck data. We conclude that our simplified Sommerfeld implementation is adequate for our general study of the mAMSB parameter space.[6]

Figure 2 illustrates the significance of the Sommerfeld enhancement via a dedicated scan of the $(m_0, m_{3/2})$ plane for $\tan\beta = 5$ using SSARD. The pink triangular region at large m_0 and relatively small $m_{3/2}$ is excluded because there are no consistent solutions to the electroweak vacuum conditions in that region. The border of that region corresponds to the line where $\mu^2 = 0$, like that often encountered in the CMSSM at low $m_{1/2}$ and large m_0 near the so-called focus-point region [105–110]. The dark blue strips indicate where the calculated $\tilde{\chi}_1^0$ density falls within the 3-σ CDM density range preferred by the Planck data [73], and the red dashed lines are contours of M_h (labelled in GeV) calculated using FeynHiggs 2.11.3.[7] The Sommerfeld enhancement is omitted in the left panel and included in the right panel of Fig. 2. We see that the Sommerfeld enhancement increases the values of $m_{3/2}$ along the prominent near-horizontal band (where the LSP is predominantly wino) by ∼200 TeV, which is much larger than the uncertainties associated with the CDM density range and our approximate implementation of the Sommerfeld enhancement. We stress that any value of $m_{3/2}$ below this band would also be allowed if the $\tilde{\chi}_1^0$ provides only a fraction of the total CDM density.

3.3.2 *Interpolation between the wino and Higgsino dark matter regions*

We note also the presence in both panels of a very narrow V-shaped diagonal strip running close to the electroweak vacuum boundary, where the $\tilde{\chi}_1^0$ LSP has a large Higgsino component as mentioned previously. As this Higgsino strip is rather difficult to see, we show in Fig. 3 a blowup of the Higgsino region for $\mu > 0$ (the corresponding region for $\mu < 0$ is similar), where we have thickened artificially the Higgsino strips by shading dark blue regions with $m_{3/2} \leq 9.1 \times 10^5$ GeV where $0.1126 \leq \Omega_{\tilde{\chi}_1^0}h^2 \leq 0.2$. As the nearly horizontal wino strip approaches the electroweak symmetry-breaking boundary, the blue strip deviates downward to a point, and then tracks the boundary back up to higher m_0 and $m_{3/2}$, forming a slanted V shape.

The origin of these two strips can be understood as follows. In most of the triangular region beneath the relatively

[6] As stated above, a full point-by-point calculation of the relic density would be impractical for our large sample of mAMSB parameters.

[7] This version is different from that used for our χ^2 evaluation, and is used here for illustration only. The numerical differences do not change the picture in a significant way.

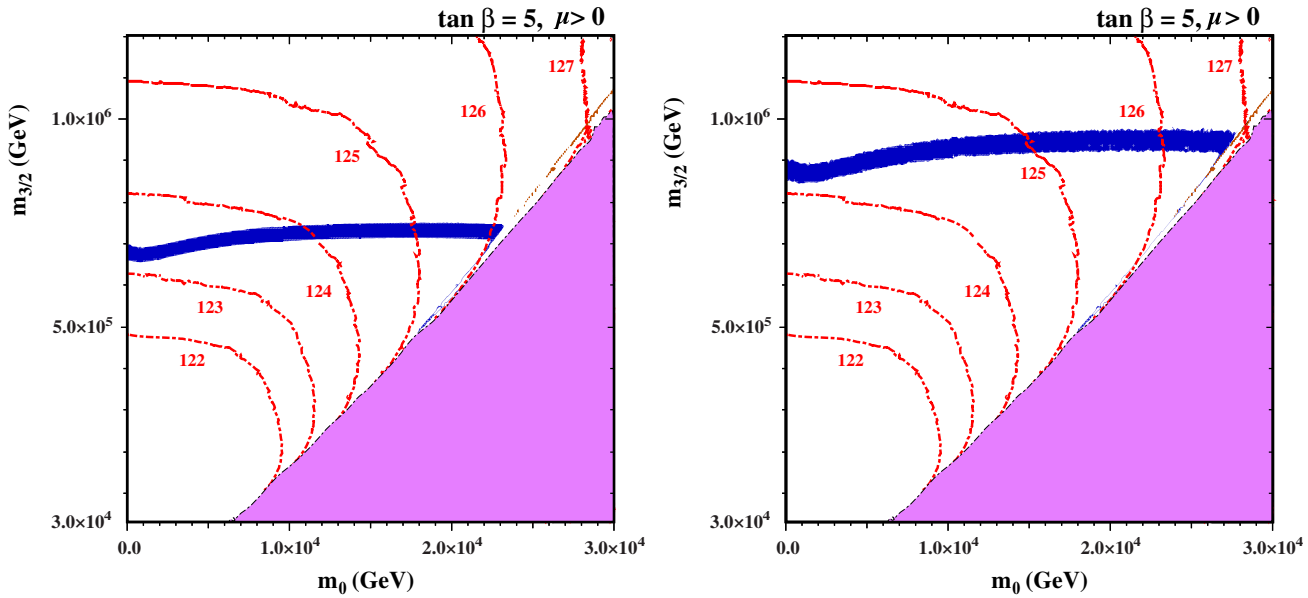

Fig. 2 The $(m_0, m_{3/2})$ plane for $\tan\beta = 5$ without (*left panel*) and with (*right panel*) the Sommerfeld enhancement, as calculated using SSARD. There are no consistent solutions of the electroweak vacuum conditions in the *pink shaded triangular regions at lower right*. The $\tilde{\chi}_1^0$ LSP density falls within the range of the CDM density indicated by Planck and other experiments in the *dark blue shaded bands*. Contours of M_h calculated using FeynHiggs 2.11.3 (see text) are shown as *red dashed lines*

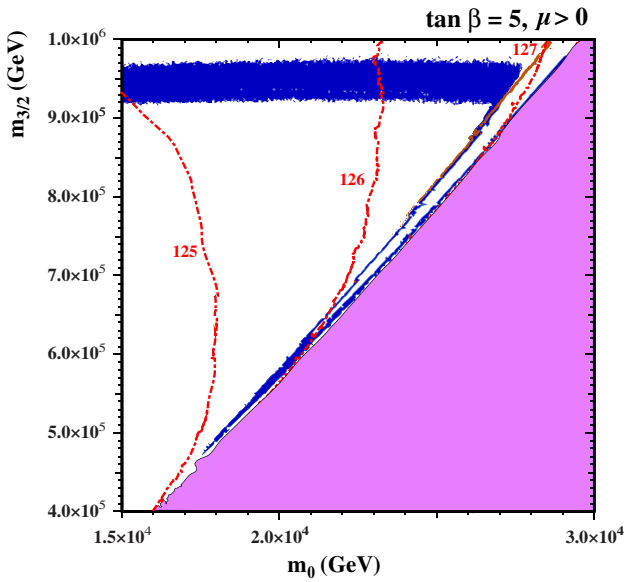

Fig. 3 Blowup of the *right panel* in Fig. 2. When $m_{3/2} \leq 9.1 \times 10^5$ GeV, we shade *dark blue regions* with $0.1126 \leq \Omega_{\tilde{\chi}_1^0} h^2 \leq 0.2$ so as to thicken the slanted V-shaped Higgsino LSP strip. Towards the upper part of the Higgsino strip, there is a *thin brown shaded strip* that is excluded because the LSP is a chargino. Contours of M_h calculated (labelled in GeV) using FeynHiggs 2.11.3 (see text) are shown as*red dashed lines*

thick horizontal strip, the LSP is a wino with mass below 3 TeV, and the relic density is below the value preferred by the Planck data. For fixed $m_{3/2}$, as m_0 is increased, μ drops so that, eventually, the Higgsino mass becomes comparable to the wino mass. When $\mu > 1$ TeV, the crossover to a Higgsino LSP (which occurs when $\mu \lesssim M_2$) yields a relic density that reaches and then exceeds the Planck relic density, producing the left arm of the slanted V-shape strip near the focus-point boundary where coannihilations between the wino and Higgsino are important. As one approaches closer to the focus point, μ continues to fall and, when $\mu \simeq 1$ TeV, the LSP becomes mainly a Higgsino and its relic density returns to the Planck range, thus producing right arm of the slanted V-shape strip corresponding to the focus-point strip in the CMSSM. In the right panel of Fig. 2 and in Fig. 3 the tip of the V where these narrow dark matter strips merge occurs when $m_0 \sim 1.8 \times 10^4$ GeV.

In the analysis below, we model the transition region by using Micromegas 3.2 [111] to calculate the relic density, with a correction in the form of an analytic approximation to the Sommerfeld enhancement given by SSARD that takes into account the varying wino and Higgsino fractions in the composition of the LSP. In this way we interpolate between the wino approximation based on SSARD discussed above for winos, and Micromegas 3.2 for Higgsinos.

Comparing the narrowness of the strips in Figs. 2 and 3 with the thickness of the near-horizontal wino strip, it is clear that they are relatively finely tuned. We also note in Fig. 3 a thin brown shaded region towards the upper part of the V-

shaped Higgsino strip that is excluded because the LSP is a chargino.

We also display in these $(m_0, m_{3/2})$ planes contours of M_h (labelled in GeV) as calculated using FeynHiggs 2.11.3 (see above). Bearing in mind the estimated uncertainty in the theoretical calculation of M_h [80], all the broad near-horizontal band and the narrow diagonal strips are compatible with the measured value of M_h, both with and without the inclusion of the Sommerfeld enhancement.

3.3.3 Dark matter detection

We implement direct constraints on the spin-independent dark matter proton scattering cross section, σ_p^{SI}, using the SSARD code (Information about this code is available from K. A. Olive: it contains important contributions from J. Evans, T. Falk, A. Ferstl, G. Ganis, F. Luo, A. Mustafayev, J. McDonald, K. A. Olive, P. Sandick, Y. Santoso, V. Spanos, and M. Srednicki.), as reviewed previously [4–8]. As discussed there and in Sect. 5.5, σ_p^{SI} inherits considerable uncertainty from the poorly constrained $\langle p|\bar{s}s|p\rangle$ matrix element and other hadronic uncertainties, which are larger than those associated with the uncertainty in the local CDM halo density.

We note also that the relatively large annihilation cross section of wino dark matter is in tension with gamma-ray observations of the Galactic centre, dwarf spheroidals and satellites of the Milky Way made by the Fermi-LAT and H.E.S.S. telescopes [112–117]. However, there are still considerable ambiguities in the dark matter profiles near the Galactic centre and in these other objects. Including these indirect constraints on dark matter annihilation in our likelihood analysis would require estimates of these underlying astrophysical uncertainties [118], which are beyond the scope of the present work.

4 Analysis procedure

4.1 MasterCode framework

We define a global χ^2 likelihood function that combines the theoretical predictions with experimental constraints, as done in our previous analyses [4–8].

We calculate the observables that go into the likelihood using the MasterCode framework [1–8] (For more information and updates, please see http://cern.ch/mastercode/.), which interfaces various public and private codes: SoftSusy 3.7.2 [119] for the spectrum, FeynHiggs 2.12.1 [80,90–94] (see Sect. 3.1) for the Higgs sector, the W boson mass and $(g-2)_\mu$, SuFla [120,121] for the B-physics observables, Micromegas 3.2 [111] (modified as discussed above) for the dark matter relic density, SSARD for the spin-independent cross section σ_p^{SI} and the wino dark matter relic density, SDECAY 1.3b [122] for calculating sparticle branching ratios, and HiggsSignals 1.4.0 [81,82] and HiggsBounds 4.3.1 [95–98] for calculating constraints on the Higgs sector. The codes are linked using the SUSY Les Houches Accord (SLHA) [123,124].

We use SuperIso [125–127] and Susy_Flavor [128] to check our evaluations of flavour observables, and we have used Matplotlib [129] and PySLHA [130] to plot the results of our analysis.

In general, we treat the observables as Gaussian constraints, combining in quadrature the experimental and applicable SM and supersymmetric theory errors, which are enumerated in Table 1 of [8]. The exceptions are $\mathrm{BR}(B_{s,d} \to \mu^+\mu^-)$ and σ_p^{SI}, for which we construct full likelihood functions combining the available data, as also described in [8].

4.2 Parameter ranges

The ranges of the mAMSB parameters that we sample are shown in Table 1. We also indicate in the right column of this Table how we divide the ranges of these parameters into segments, as we did previously for our analyses of the CMSSM, NUHM1, NUHM2, pMSSM10 and SU(5) [4–8]. The combinations of these segments constitute boxes, in which we sample the parameter space using the MultiNest package [131–133]. For each box, we choose a prior for which 80% of the sample has a flat distribution within the nominal range, and 20% of the sample is outside the box in normally distributed tails in each variable. In this way, our total sample exhibits a smooth overlap between boxes, eliminating spurious features associated with box boundaries. Since it is relatively fine-tuned, we made a dedicated supplementary 36-box scan of the Higgsino-LSP region of the mAMSB parameter space, requiring the lightest neutralino to be Higgsino-like. We have sampled a total of $11(13) \times 10^6$ points for $\mu > 0$ ($\mu < 0$).

Table 1 Ranges of the mAMSB parameters sampled, together with the numbers of segments into which each range was divided, and the corresponding number of sample boxes. The numbers of segments and boxes are shown both for the generic scan and for the supplementary scan where we constrain the neutralino to be Higgsino-like

Parameter	Range	Generic segments	Higgsino segments
m_0	(0.1, 50 TeV)	4	6
$m_{3/2}$	(10, 1500 TeV)	3	3
$\tan\beta$	(1, 50)	4	2
Total number of boxes		48	36

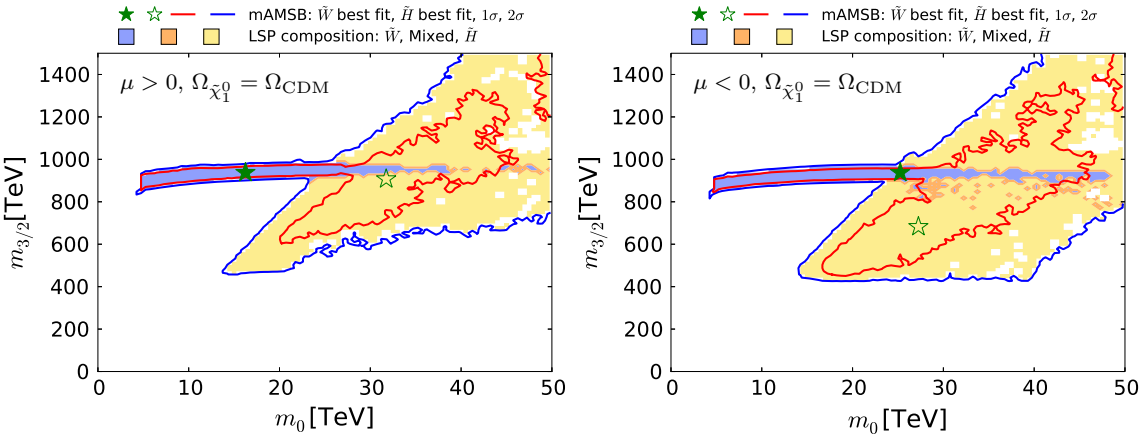

Fig. 4 The $(m_0, m_{3/2})$ planes for $\mu > 0$ (*left panel*) and $\mu < 0$ (*right panel*). The *red and blue coloured contours* surround regions that are allowed at the 68 and 95% confidence levels (CLs), corresponding approximately to one and two standard deviations, respectively, assuming that all the CDM is provided by the $\tilde{\chi}_1^0$. The wino-like (Higgsino-like) DM regions are *shaded blue* (*yellow*), and mixed wino–Higgsino regions are *shaded orange*. The best-fit points for the two signs of μ are indicated by *green stars*, closed in the wino-like region and open in the Higgsino-like region

5 Results

5.1 Case I: CDM is mainly the lightest neutralino

We display in Fig. 4 the $(m_0, m_{3/2})$ planes for our sampling of mAMSB parameters with $\mu > 0$ (left panel) and $\mu < 0$ (right panel). The coloured contours bound regions of parameter space with $\Delta\chi^2 = 2.30$ and $\Delta\chi^2 = 5.99$ contours, which we use as proxies for the boundaries of the 68% (red) and 95% (dark blue) CL regions. The best-fit points for the two signs of μ are indicated by green stars, closed in the case of wino-like DM, open in the case of Higgsino-like DM. The shadings in this and subsequent planes indicate the composition of the sample point with the lowest χ^2 in this projection: in general, there will also be sample points with a different composition and (possibly only slightly) larger χ^2. Different shading colours represent the composition of the $\tilde{\chi}_1^0$ LSP: a region with Higgsino fraction exceeding 90% is shaded yellow, one with wino fraction exceeding 90% is shaded light blue, while other cases are shaded orange.[8] Most of blue shading corresponds to a wino-like LSP, and in only a small fraction of cases to a mixed wino–Higgsino state. We see that in the case of a wino-like LSP, the regions favoured at the 2-σ level are bands with 900 TeV $\lesssim m_{3/2} \lesssim$ 1000 TeV corresponding to the envelope of the near-horizontal band in the right panel of Fig. 2 and in Fig. 3 that is obtained when profiling over $\tan\beta$. For both signs of μ, the lower limit $m_0 \gtrsim 5$ TeV is due to the $\tilde{\tau}_1$ becoming the LSP.

The yellow Higgsino-LSP regions correspond to the envelope of the V-shaped diagonal strips seen in Fig. 2 and in Fig. 3. The locations of these diagonal strips vary significantly with $\tan\beta$ and m_t, and their extents are limited at small and large gravitino mass mainly by the Higgs mass constraint. The best-fit point for the Higgsino-LSP scenario has a total χ^2 very similar to the wino-LSP case, as is shown in Fig. 5. The χ^2 values at the best-fit points in the wino- and Higgsino-like regions for both signs of μ are given in Table 2, together with more details of the fit results (see below).

Figures 6 and 7 display the $(\tan\beta, m_0)$ and $(\tan\beta, m_{3/2})$ planes, respectively. Both the $\mu > 0$ case (left panel) and the $\mu < 0$ case (right panel) are shown, and are qualitatively similar. The best-fit points for the two signs of μ are again indicated by green stars. Larger m_0 and $m_{3/2}$ values are allowed in the Higgsino-LSP case, provided that $\tan\beta$ is small. Values of $\tan\beta \gtrsim 3$ are allowed at the 95% CL with an upper limit at 48 only in the $\mu > 0$ case. There are regions favoured at the 68% CL with small values of $\tan\beta \lesssim 10$ in both the wino- and Higgsino-like cases for both signs of μ. In addition, for $\mu > 0$ there is another 68% CL preferred region in the wino case at $\tan\beta \gtrsim 35$, where supersymmetric contributions improve the consistency with the measurements of BR$(B_{s,d} \to \mu^+\mu^-)$, as discussed in more detail in Sect. 5.3.[9]

The parameters of the best-fit points for $\mu > 0$ and $\mu < 0$ are listed in Table 2, together with their 68% CL ranges corresponding to $\Delta\chi^2 = 1$. We see that at the 68% CL the range of $\tan\beta$ is restricted to low values for both

[8] The uncoloured patches and the irregularities in the contours are due to the limitations of our sampling.

[9] The diagonal gap in the left panel of Fig. 7 for $\mu > 0$ is in a region where our numerical calculations encounter instabilities.

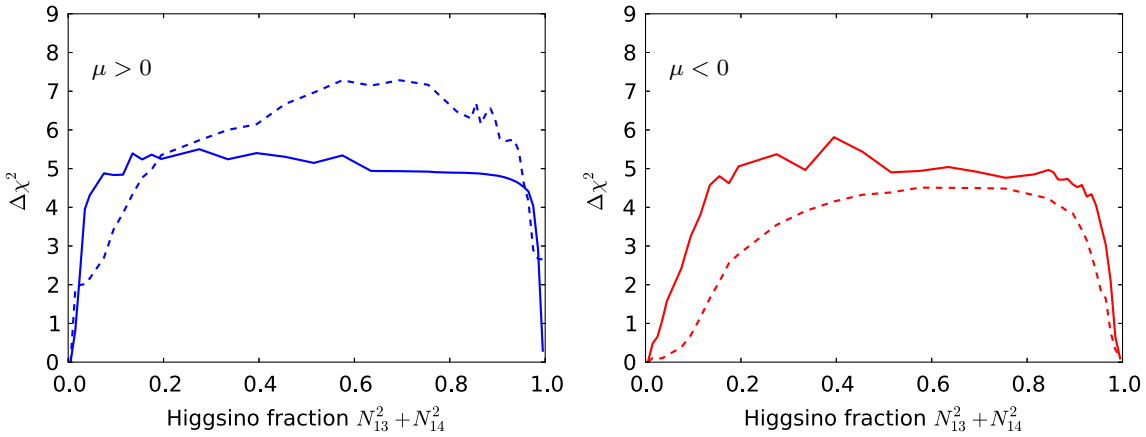

Fig. 5 Profiled $\Delta\chi^2$ of the $\tilde{\chi}_1^0$ Higgsino fraction for $\mu > 0$ (*left panel*) and for $\mu < 0$ (*right panel*). The profiles for the $\Omega_{\tilde{\chi}_1^0} = \Omega_{\rm CDM}$ case and for the $\Omega_{\tilde{\chi}_1^0} \leq \Omega_{\rm CDM}$ case are shown as *solid* and *dashed lines*, respectively. The lowest-χ^2 point in the Higgsino-LSP region ($N_{13}^2 + N_{14}^2 \simeq 1$) has very similar χ^2 to the wino-LSP best-fit point ($N_{13}^2 + N_{14}^2 \simeq 0$), except in the $\mu > 0$ $\Omega_{\tilde{\chi}_1^0} \leq \Omega_{\rm CDM}$ case

Table 2 Fit results for the mAMSB assuming that the LSP makes the dominant contribution to the cold dark matter density. The 68% CL ranges correspond to $\Delta\chi^2 = 1$. We also display the values of the global χ^2 function omitting the contributions from `HiggsSignals`, and the corresponding χ^2 probability values calculated taking into account the relevant numbers of degrees of freedom (including the electroweak precision observables) using the standard prescription [82]. Each mass range is shown for both the wino- and Higgsino-LSP scenarios as well as for both signs of μ

Parameter	Wino-LSP		Higgsino-LSP	
	$\mu > 0$	$\mu < 0$	$\mu > 0$	$\mu < 0$
m_0: best-fit value	16 TeV	25 TeV	32 TeV	27 TeV
68% range	(4, 40) TeV	(4, 43) TeV	(23, 50) TeV	(18, 50) TeV
$m_{3/2}$: best-fit value	940 TeV	940 TeV	920 TeV	650 TeV
68% range	(860, 970) TeV	(870, 950) TeV	(650, 1500) TeV	(480, 1500) TeV
$\tan\beta$: best-fit value	5.0	4.0	4.4	4.2
68% range	(3, 8) and (42, 48)	(3, 7)	(3, 7)	(3, 7)
χ^2/d.o.f	36.4/27	36.4/27	36.6/27	36.4/27
χ^2 probability	10.7%	10.7%	10.2%	10.7%

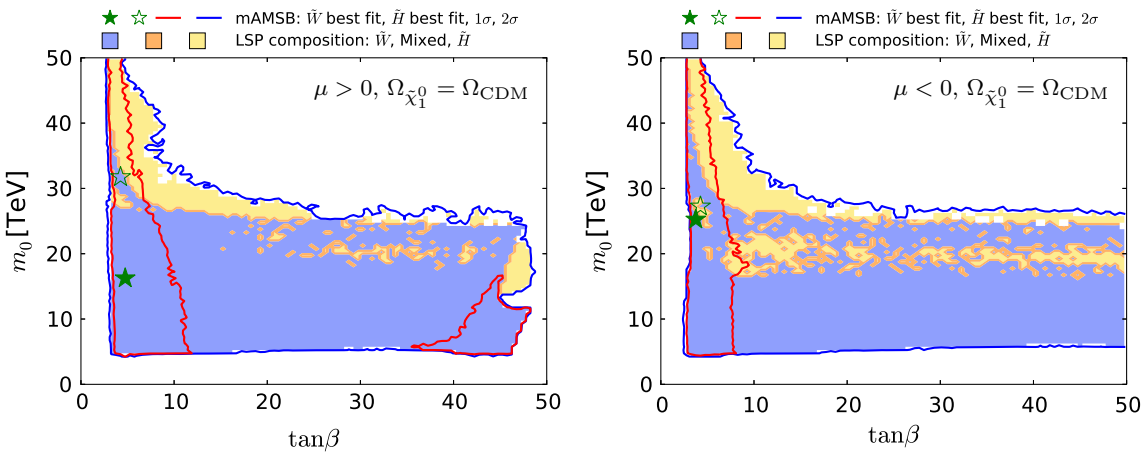

Fig. 6 The $(\tan\beta, m_0)$ planes for $\mu > 0$ (*left panel*) and for $\mu < 0$ (*right panel*), assuming that the $\tilde{\chi}_1^0$ provides all the CDM density. The colouring convention for the shadings and contours is the same as in Fig. 4, and the best-fit points for the two signs of μ are again indicated by *green stars*

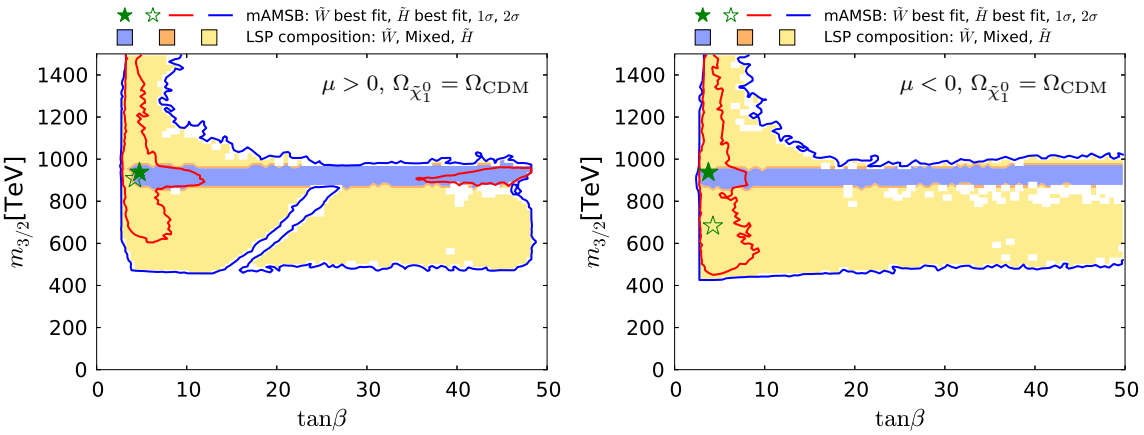

Fig. 7 The (tan β, $m_{3/2}$) planes for $\mu > 0$ (*left panel*) and $\mu < 0$ (*right panel*), assuming that the $\tilde{\chi}_1^0$ provides all the CDM density. The shadings and colouring convention for the contours are the same as in Fig. 4, and the best-fit points for the two signs of μ are again indicated by *green stars*

LSP compositions, with the exception of the $\mu > 0$ wino-LSP case, where also larger tan β values around 45 are allowed. In the wino-LSP scenario, $m_{3/2}$ is restricted to a narrow region around 940 TeV and m_0 is required to be larger than 4 TeV. The precise location of the Higgsino-LSP region depends on the spectrum calculator employed, and also on the version used. These variations can be as large as tens of TeV for m_0 or a couple of units for tan β, and can change the χ^2 penalty coming from the Higgs mass. In our implementations, we find that $m_{3/2}$ can take masses as low as 650 TeV (480 TeV) while m_0 is required to be at least 23 TeV (18 TeV) at the 68% CL in the $\mu > 0$ ($\mu < 0$) case. This variability is related to the uncertainty in the exact location of the electroweak symmetry-breaking boundary, which is very sensitive to numerous corrections, in particular those related to the top quark Yukawa coupling.

The minimum values of the global χ^2 function for the two signs of μ are also shown in Table 2, as are the χ^2 probability values obtained by combining these with the numbers of effective degrees of freedom. We see that all the cases studied (wino- and Higgsino-like LSP, $\mu > 0$ and $\mu < 0$) have similar χ^2 probabilities, around 11%, calculated taking into account the relevant numbers of degrees of freedom (including the electroweak precision observables) using the standard prescription [82].

We show in Fig. 8 the contributions to the total χ^2 of the best-fit point in the scenarios with different hypotheses on the sign of μ and the composition of CDM. In addition, we report the main χ^2 penalties in Table 3.

Figure 9 shows the best-fit values (blue lines) of the particle masses and the 68 and 95% CL ranges allowed in both the wino- and Higgsino-like LSP cases for both signs of μ. More complete spectra at the best-fit points for the two signs of μ are shown in Fig. 10 in both the wino- and Higgsino-LSP cases, where branching ratios exceeding 20% are indicated by dashed lines. As was apparent from the previous figures and tables, a relatively heavy spectrum is favoured in our global fits. The difference between the best-fit spectra in the Higgsino LSP case for $\mu > 0$ and < 0 reflects the fact that the likelihood function is quite flat in the preferred region of the parameter space. In the Higgsino-LSP case, the spectra are even heavier than the other one with a wino LSP, apart from the gauginos, which are lighter. Overall, these high-mass scales, together with the minimal flavor violation assumption, implies that there are, in general, no significant departures from the SM predictions in the flavour sector or for $(g-2)_\mu$.

Figure 11 shows the (M_A, tan β) planes for $\mu > 0$ (left panel) and for $\mu < 0$ (right panel), assuming that the $\tilde{\chi}_1^0$ contributes all the CDM density. As previously, the red (blue) contours represent the 68% (95%) CL contours, and the wino-like (Higgsino-like) DM regions are shaded blue (yellow), and mixed wino–Higgsino regions are shaded orange. We find that the impact of the recent LHC 13-TeV constraints on the (M_A, tan β) plane is small in these plots. We see here that the large-tan β 68% CL region mentioned above corresponds to $M_{\rm A} \lesssim 6$ TeV.

As anticipated in Sect. 1, the wino-LSP is almost degenerate with the lightest chargino, which acquires a mass about 170 MeV larger through radiative corrections. Therefore, because of phase-space suppression the chargino acquires a lifetime around 0.15 ns, and therefore may decay inside the ATLAS tracker. However, the ATLAS search for disappearing tracks [134] is insensitive to the large mass ∼2.9 TeV expected for the mAMSB chargino if the LSP makes up all the dark matter. In Sect. 5.2 we estimate the LHC sensitivity to the lower chargino masses that are possible if the $\tilde{\chi}_1^0$

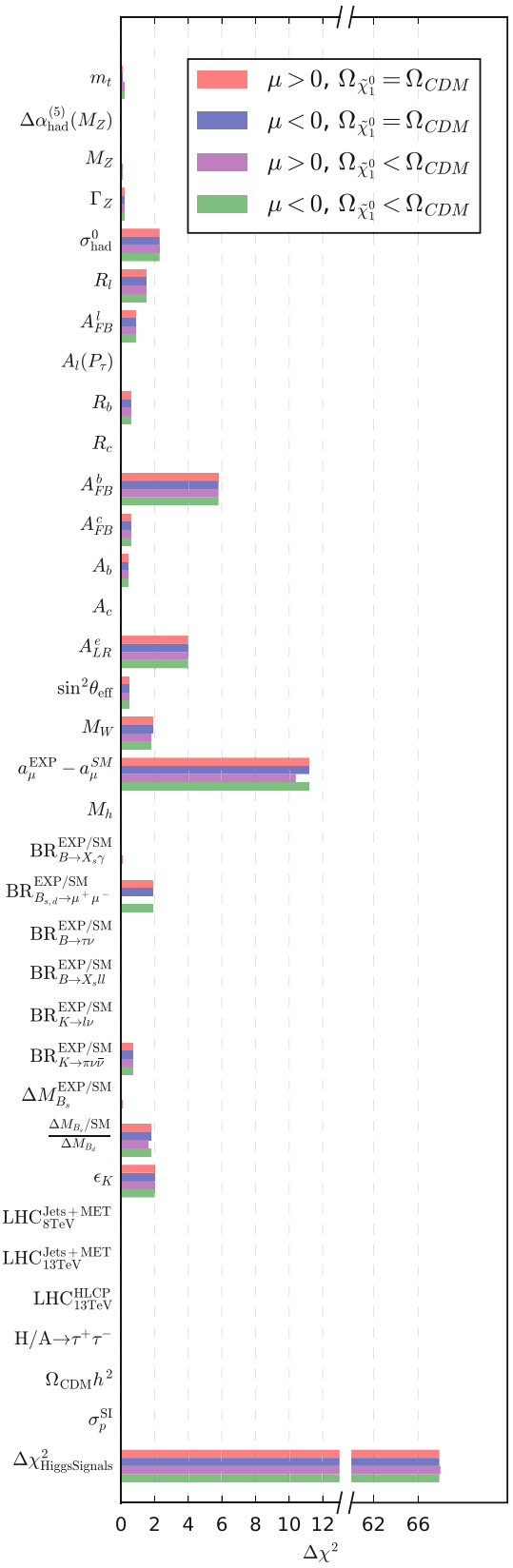

Fig. 8 All the contributions to the total χ^2 for the best-fit points for mAMSB assuming different hypotheses on the composition of the dark matter relic density and on the sign of μ as indicated in the legend

contributes only a fraction of the cold dark matter density. In the Higgsino-LSP case, the chargino has a mass ∼1.1 TeV in the all-DM case, but its lifetime is very short, of the order of few ps.

The 68% CL ranges of the neutralino masses, the gluino mass, the $\tilde{\chi}_1^\pm - \tilde{\chi}_1^0$ mass splitting and the $\tilde{\chi}_1^\pm$ lifetime are reported in Table 4, assuming that the $\tilde{\chi}_1^0$ accounts for all the CDM density. Each parameter is shown for both the wino- and Higgsino-like LSP scenarios and for the two signs of μ.

Figure 12 shows our results in the $(m_{\tilde{\chi}_1^0}, \Omega_{\tilde{\chi}_1^0}h^2)$ plane in the case when the $\tilde{\chi}_1^0$ is required to provide all the CDM density, within the uncertainties from the Planck and other measurements. The left panel is for $\mu > 0$ and the right panel is for $\mu < 0$: they are quite similar, with each featuring two distinct strips. The strip where $m_{\tilde{\chi}_1^0} \sim 1$ TeV corresponds to a Higgsino LSP near the focus-point region, and the strip where $m_{\tilde{\chi}_1^0} \sim 3$ TeV is in the wino LSP region of the parameter space. In between these strips, the make-up of the LSP changes as the wino- and Higgsino-like neutralino states mix, and coannihilations between the three lightest neutralinos and both charginos become important. The Sommerfeld enhancement varies rapidly (we recall that it is not important in the Higgsino LSP region), causing the relic density to rise rapidly as well. We expect the gap seen in Fig. 12 to be populated by points with very specific values of m_0.

5.2 Case II: the LSP does not provide all the cold dark matter

If the LSP is not the only component of the cold dark matter, $m_{\tilde{\chi}_1^0}$ may be smaller, $m_{3/2}$ may also be lowered substantially, and some sparticles may be within reach of the LHC. The preferred regions of the $(m_0, m_{3/2})$ planes for $\mu > 0$ (left panel) and $\mu < 0$ (right panel) in this case are shown in the upper panels of Fig. 13.[10] We see that the wino region allowed at the 95% CL extends to smaller $m_{3/2}$ for both signs of μ, and also to larger m_0 at $m_{3/2} \gtrsim 300$ TeV when $\mu < 0$. We also see that the 68% CL region extends to much larger m_0 and $m_{3/2}$ when $\mu < 0$, and the best-fit point also moves to larger masses than for $\mu > 0$, though with smaller $\tan\beta$.

The best-fit points and mass ranges for the case where the LSP relic density falls below the Planck preferred density are given in Table 5. As one can see, the best fit for $\mu > 0$ has a somewhat lower value of χ^2 and a significantly higher value of $\tan\beta$. This is because in the case

[10] The sharp boundaries at low m_0 in the upper panels of Fig 13 are due to the stau becoming the LSP, and the narrow separation between the near-horizontal portions of the 68 and 95% CL contours in the upper right panel of Fig. 13 is due to the sharp upper limit on the CDM density.

Table 3 The most important contributions to the total χ^2 of the best-fit points for mAMSB assuming different hypotheses on the composition of the dark matter relic density and on the sign of μ. In the $\mu > 0$ scenario with $\Omega_{\tilde{\chi}_1^0} < \Omega_{\rm CDM}$ and $\tilde{W}$-LSP, the experimental constraints from $(g-2)_\mu$ and ${\rm BR}(B_s \to \mu^+\mu^-)$ can be accommodated and get a lower χ^2 penalty

Constraint	$\Omega_{\tilde{\chi}_1^0} = \Omega_{\rm CDM}$				$\Omega_{\tilde{\chi}_1^0} < \Omega_{\rm CDM}$			
	$\tilde{W}$-LSP		$\tilde{H}$-LSP		$\tilde{W}$-LSP		$\tilde{H}$-LSP	
	$\mu > 0$	$\mu < 0$	$\mu > 0$	$\mu < 0$	$\mu > 0$	$\mu < 0$	$\mu > 0$	$\mu < 0$
$\sigma^0_{\rm had}$	2.3	2.3	2.3	2.3	2.3	2.3	2.3	2.3
R_l	1.5	1.5	1.5	1.5	1.5	1.5	1.5	1.5
$A^b_{\rm FB}$	5.8	5.8	5.8	5.8	5.8	5.8	5.8	5.8
$A^e_{\rm LR}$	4.0	4.0	4.0	4.0	4.0	4.0	4.0	4.0
M_W	1.9	1.9	2.1	1.9	1.8	1.8	1.8	1.9
$(g-2)_\mu$	11.2	11.2	11.2	11.2	10.4	11.2	11.2	11.2
${\rm BR}(B_s \to \mu^+\mu^-)$	1.9	1.9	1.9	1.9	0.0	1.9	1.9	1.9
$\frac{\Delta M_{B_s}/{\rm SM}}{\Delta M_{B_d}}$	1.8	1.8	1.8	1.8	1.6	1.8	1.8	1.8
ϵ_K	2.0	2.0	2.0	2.0	2.0	2.0	2.0	2.0
$\Delta\chi^2_{\rm HiggsSignals}$	67.9	67.9	67.9	68.0	68.0	67.9	67.9	68.0

of positive μ there is negative interference between the mAMSB and SM contributions to the decay amplitude in this parameter-space region, reducing ${\rm BR}(B_{s,d} \to \mu^+\mu^-)$ and allowing a better fit to the latest experimental combination of ATLAS, CMS and LHCb measurements (see Fig. 19). On the other hand, in the negative-μ case, the interference is constructive and thus the best fit to the experimental measurement is for a SM-like branching ratio, which is predicted in a much wider region of the parameter space. As previously, the quoted χ^2 probabilities are calculated taking into account the relevant numbers of degrees of freedom (including the electroweak precision observables) using the standard prescription [82].

The lower panels of Fig. 13 show the $(\tan\beta, m_{3/2})$ planes for $\mu > 0$ (left) and for $\mu < 0$ (right). Comparing with the corresponding planes in Fig. 7 for the case in which the LSP provides all the dark matter, we see a large expansion of the wino-like region, we note that the allowed range of $m_{3/2}$ extends down to $\sim$ 100 TeV, and the 68% CL region is found to extend to large values of $\tan\beta$.

We display in Fig. 14 the $(M_{\rm A}, \tan\beta)$ planes in the partial-CDM case for $\mu > 0$ (left panel) and $\mu < 0$ (right panel). Comparing with the corresponding Fig. 11 for the all-CDM case, we see that a large region of smaller values of $M_{\rm A}$ and $\tan\beta$ are allowed in this case. We also note that the best-fit point in the wino-like region for $\mu > 0$ has moved to a much smaller value of $M_{\rm A}$ and a much larger value of $\tan\beta$, much closer to the region currently excluded by LHC searches. In this connection, we note that the fit including only the LHC 8-TeV $H/A \to \tau^+\tau^-$ constraint [99] is slightly weaker in this region than that including the 13-TeV constraint [100]. This gives hope that future improvements in the LHC H/A search may be sensitive to the preferred region of the mAMSB parameter space in the partial-CDM case.

Figure 15 displays the $(m_{\tilde{\chi}_1^0}, \Omega_{\tilde{\chi}_1^0}h^2)$ planes for $\mu > 0$ (left panel) and $\mu < 0$ (right panel) in the partial-CDM case. We see that the allowed range of $\tilde{\chi}_1^0$ masses decreases with $\Omega_{\tilde{\chi}_1^0}h^2$, as expected. Pure wino or Higgsino LSP states are slightly preferred over mixed ones because the latter are accompanied by larger scattering cross sections on protons and are thus in tension with direct DM searches (see Sect. 5.5). The preferred region in the wino-like LSP $\mu > 0$ case appears at small values of $m_{\tilde{\chi}_1^0}$ and $\Omega_{\tilde{\chi}_1^0}h^2$, pulled down by the possibility of negative interference in the $B_{s,d} \to \mu^+\mu^-$ decay amplitudes and the consequent decrease in ${\rm BR}(B_{s,d} \to \mu^+\mu^-)$, as discussed in Section 5.3. In the Higgsino-LSP $\mu > 0$ case and in all $\mu < 0$ cases, all $\Omega_{\tilde{\chi}_1^0}h^2$ values below the Planck preferred density are equally likely.

Figure 16 shows the mass spectra allowed in the wino-like LSP case for $\mu > 0$ (top panel) and $\mu < 0$ (second panel), and also in the Higgsino-like LSP case for $\mu > 0$ (third panel) and $\mu < 0$ (bottom panel). The one- and two-σ ranges are again shown in dark and light orange respectively, and the best-fit values are represented by blue lines. We see that the spectra in the wino-like LSP case are quite different for the two signs of μ, whereas those in the Higgsino-like LSP case resemble each other more. Table 6 provides numerical values for the 68% CL ranges for the neutralino masses, the gluino mass, the mass difference between the lightest chargino and neutralino, as well as for the corresponding chargino lifetime.

Finally, Fig. 17 displays the spectra of our best-fit points in the case that the LSP contributes only a fraction of the cold dark matter density. As previously, the left panels are for $\mu > 0$ and the right panels are for $\mu < 0$ (note the different scales on the vertical axes). Both the wino- (upper) and the Higgsino-like LSP (lower) best-fit points are shown. In each

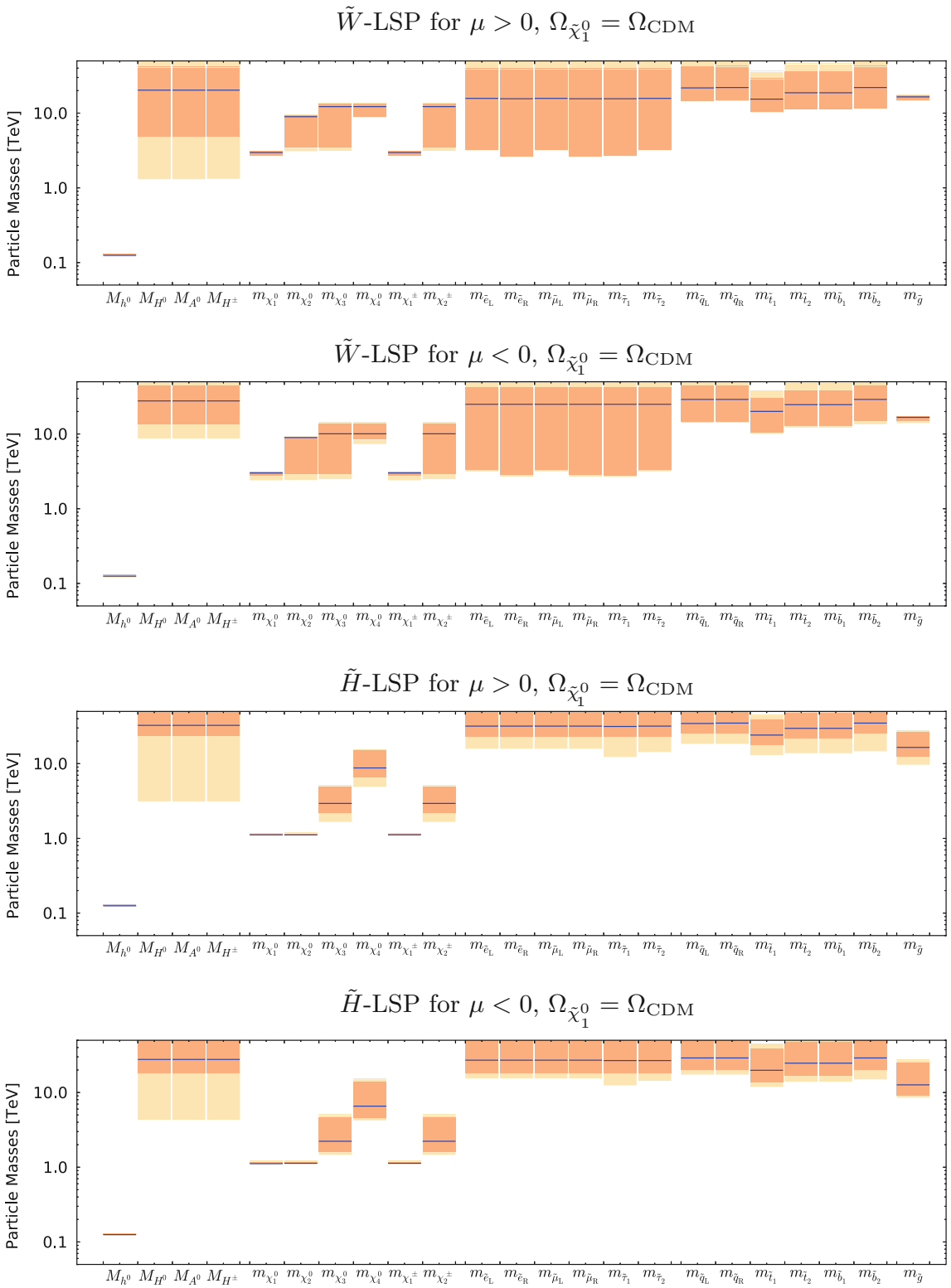

Fig. 9 The ranges of masses obtained for the wino-like LSP case with $\mu > 0$ (*top panel*) and $\mu < 0$ (*second panel*), and also for the Higgsino-like LSP case for $\mu > 0$ (*third panel*) and $\mu < 0$ (*bottom panel*), assuming that the LSP makes the dominant contribution to the cold dark matter density

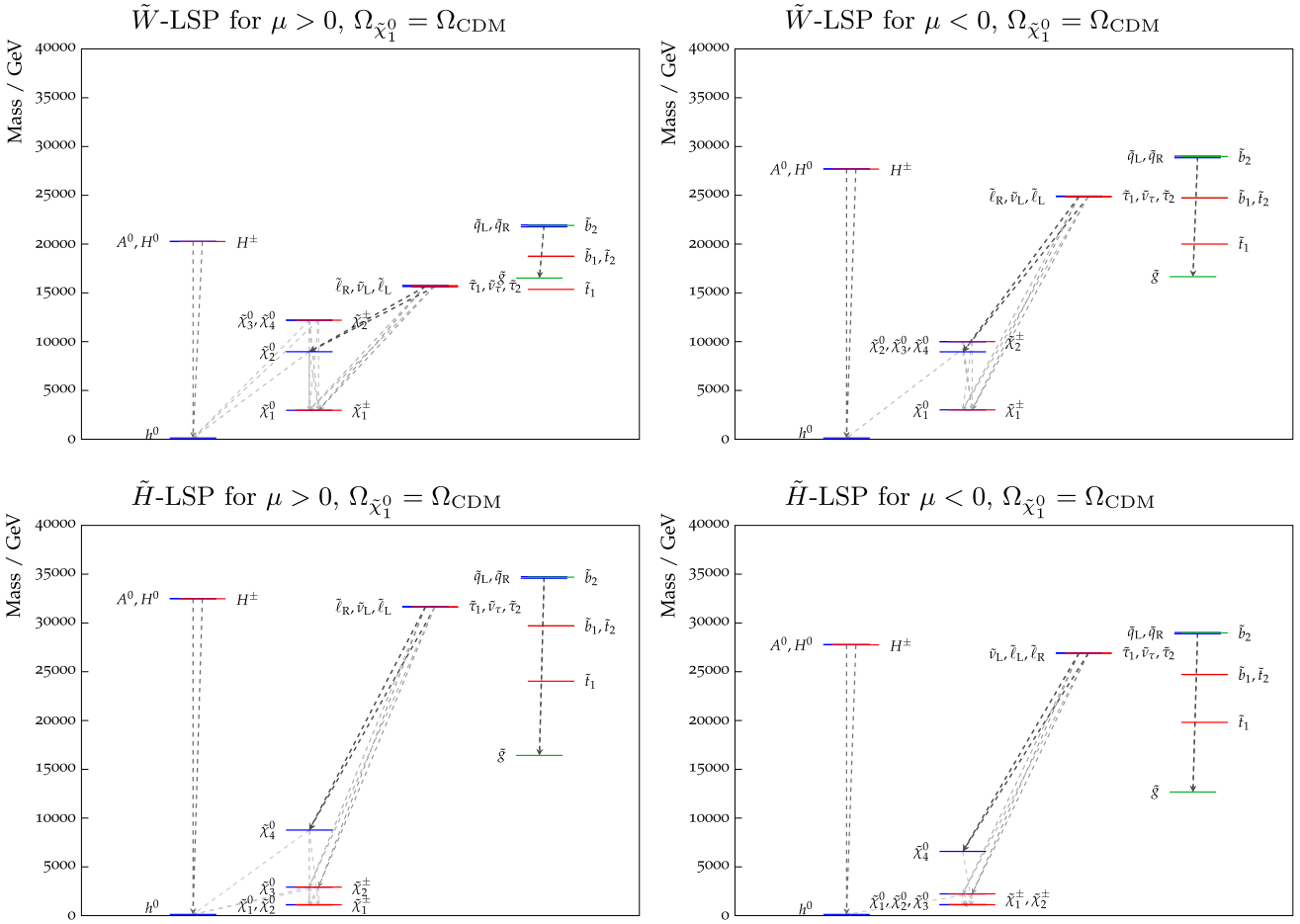

Fig. 10 The spectra of our best-fit points for $\mu > 0$ (*left panel*) and $\mu < 0$ (*right panel*), assuming that the LSP makes the dominant contribution to the cold dark matter density. Both the wino-like (*upper*) and the Higgsino-like LSP (*lower*) best-fit points are shown. In each case, we also indicate all the decay modes with branching ratios (BRs) above 20%, with *darker shading* for larger BRs, and the *colours of the horizontal bars* reflect particles electric charges

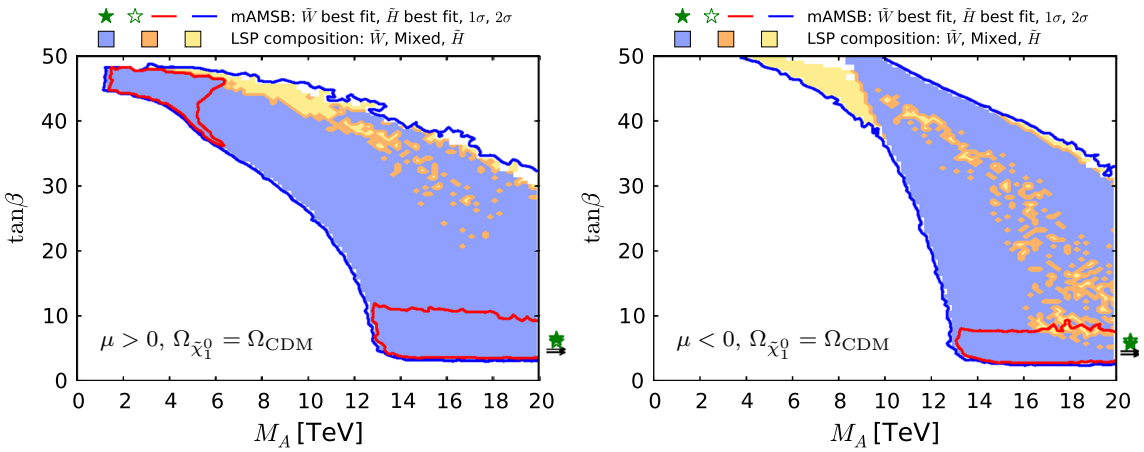

Fig. 11 The $(M_A, \tan\beta)$ planes for $\mu > 0$ (*left panel*) and for $\mu < 0$ (*right panel*), assuming that the $\tilde{\chi}_1^0$ contributes all the CDM density. As previously, the *red* (*blue*) *contours* represent the 68% (95%) CL contours, and the wino-like (Higgsino-like) (mixed wino–Higgsino) DM regions are *shaded blue* (*yellow*) (*orange*)

Table 4 The 68% CL ranges for the masses of the LSP $\tilde{\chi}_1^0$ and of the heavier neutralinos $\tilde{\chi}_2^0$, $\tilde{\chi}_3^0$ and $\tilde{\chi}_4^0$, as well as the mass splitting between the lighter chargino $\tilde{\chi}_1^\pm$ and the LSP and the corresponding lifetime of the $\tilde{\chi}_1^\pm$, for the case in which the $\tilde{\chi}_1^0$ accounts for all the CDM density. Each parameter is shown for both the wino- and Higgsino-LSP scenarios, as well as for both signs of μ

Parameter	wino-LSP		Higgsino-LSP	
	$\mu > 0$	$\mu < 0$	$\mu > 0$	$\mu < 0$
$m_{\tilde{\chi}_1^0}$	2.9 ± 0.1 TeV	2.9 ± 0.1 TeV	1.12 ± 0.02 TeV	1.13 ± 0.02 TeV
$m_{\tilde{\chi}_2^0}$	(3.4, 9.2) TeV	(2.9, 9.1) TeV	1.13 ± 0.02 TeV	1.14 ± 0.02 TeV
$m_{\tilde{\chi}_3^0}$	(3.5, 13.5) TeV	(2.9, 13.5) TeV	(2.2, 4.9) TeV	(1.7, 4.6) TeV
$m_{\tilde{\chi}_4^0}$	(9.0, 13.5) TeV	(8.4, 13.5) TeV	(6.5, 15.0) TeV	(4.6, 14.0) TeV
$m_{\tilde{g}}$	16 ± 1 TeV	16 ± 1 TeV,	(13, 26) TeV	(9, 25) TeV
$m_{\tilde{\chi}_1^\pm} - m_{\tilde{\chi}_1^0}$	0.17 ± 0.01 GeV	0.17 ± 0.01 GeV	(0.7, 1.3) GeV	(1.3, 2.2) GeV
$\tau_{\tilde{\chi}_1^\pm}$	0.15 ± 0.02 ns	0.15 ± 0.02 ns	$<5.0 \times 10^{-3}$ ns	$<1.0 \times 10^{-3}$ ns

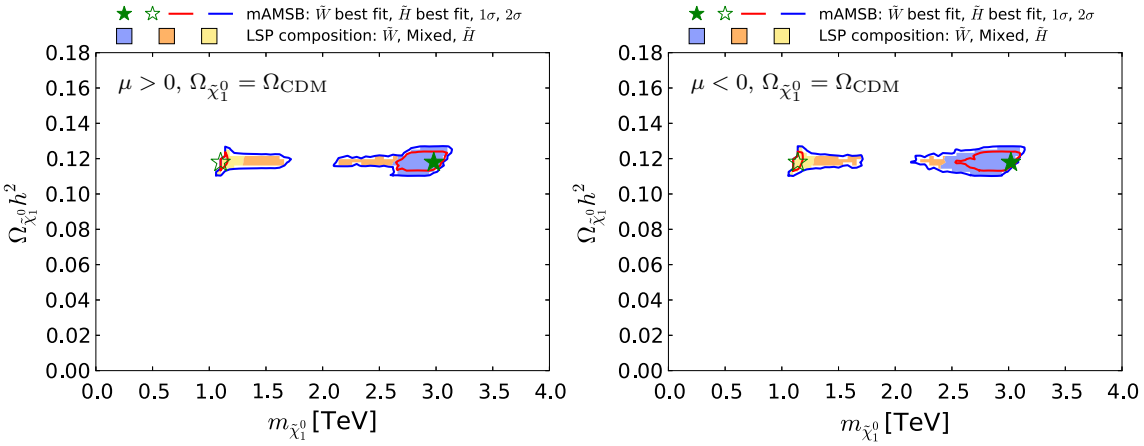

Fig. 12 The $(m_{\tilde{\chi}_1^0}, \Omega_{\tilde{\chi}_1^0} h^2)$ planes for $\mu > 0$ (*left panel*) and $\mu < 0$ (*right panel*) assuming that all the CDM density is provided by the $\tilde{\chi}_1^0$. The shadings are the same as in Fig. 4

case, we also indicate all the decay modes with branching ratios above 20%.

5.3 χ^2 likelihood functions for observables

We show in Fig. 18 the one-dimensional likelihoods for several sparticle masses. In all cases the solid lines correspond to the case in which the LSP accounts for all of the CDM, and the dashed lines for the case in which it may provide only a fraction of the CDM. The blue lines are for $\mu > 0$ and the red lines are for $\mu < 0$. It is apparent that in the all-CDM case the sparticles in the mAMSB are expected to be too heavy to be produced at the LHC: $m_{\tilde{g}}, m_{\tilde{t}_1} \gtrsim 10$ TeV, $m_{\tilde{q}} \gtrsim 15$ TeV, $m_{\tilde{\tau}_1} \gtrsim 3$ TeV, $m_{\tilde{\chi}_1^0} \gtrsim 1$ TeV. However, in the part-CDM case the sparticle masses may be much lighter, with strongly interacting sparticles possibly as light as ~ 2 TeV and much lighter $\tilde{\chi}_3^0$ and $\tilde{\chi}_2^\pm$ also possible, so that some of them may become accessible at LHC energies. Indeed, as we discuss below, future LHC runs should be able to explore parts of the allowed parameter space.

As shown in Fig. 19, there are some interesting prospects for indirect searches for mAMSB effects. There are in general small departures from the SM if the LSP accounts for all of the CDM, whereas much more significant effects can arise if the CDM constraint is relaxed. In particular, we find that significant destructive interference between mAMSB effects and the SM may cause a sizeable decrease of the BR($B_{s,d} \to \mu^+\mu^-$) branching ratio in the positive μ case, which can be significant within the range of model parameters allowed at the 2-σ level and improves the agreement with the experimental measurement shown by the dotted line. This effect arises from a region of parameter space at large tan β where $M_{\rm A}$ can be below 5 TeV, as seen in the bottom right panel of Fig. 18. We find that the destructive interference in BR($B_{s,d} \to \mu^+\mu^-$) is always accompanied by a constructive interference in BR($b \to s\gamma$). There is also some possibility of positive interference in BR($B_{s,d} \to \mu^+\mu^-$) and negative interference in BR($b \to s\gamma$) when $\mu < 0$ and the LSP does not provide all the dark matter, though this effect is much smaller. Finally, we also note that only small effects at the level of 10^{-10} can appear in $(g-2)_\mu$, for either sign of μ.

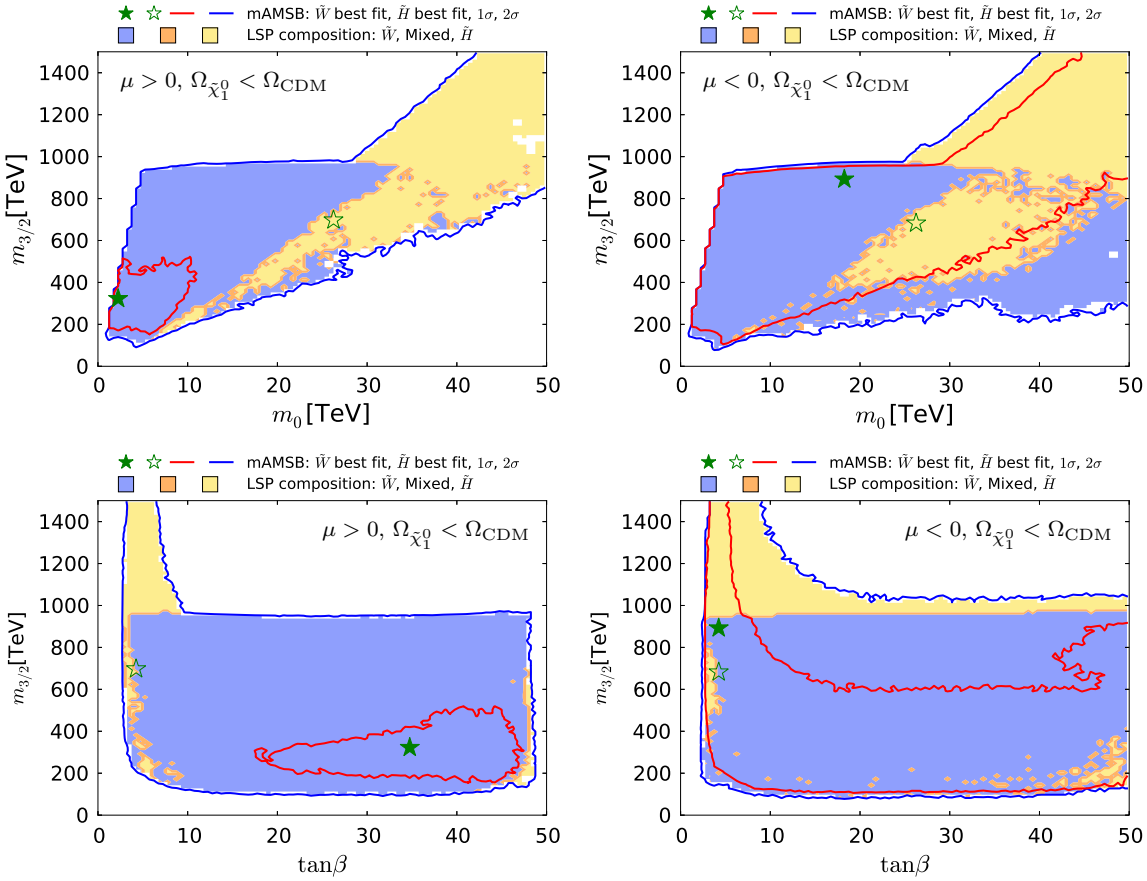

Fig. 13 The $(m_0, m_{3/2})$ planes (*upper panels*) and the $(\tan\beta, m_{3/2})$ planes (*lower panels*) for $\mu > 0$ (*left panels*) and for $\mu < 0$ (*right panels*), allowing the $\tilde{\chi}_1^0$ to contribute only part of the CDM density. The shadings are the same as in Fig. 4

Table 5 Fit results for the mAMSB assuming that the LSP accounts for just a fraction of the cold dark matter density. The 68% CL ranges correspond to $\Delta\chi^2 = 1$. We also display the values of the global χ^2 function omitting the contributions from `HiggsSignals`, and the corresponding χ^2 probability values calculated taking into account the relevant numbers of degrees of freedom (including the electroweak precision observables) using the standard prescription [82]. Each mass range is shown for both the wino- and Higgsino-LSP scenarios and both signs of μ

Parameter	Wino-LSP		Higgsino-LSP	
	$\mu > 0$	$\mu < 0$	$\mu > 0$	$\mu < 0$
m_0: best-fit value	2.0 TeV	18 TeV	26 TeV	26 TeV
68% range	(1, 8) TeV	(1, 40) TeV	(6, 50) TeV	(6, 50) TeV
$m_{3/2}$: best-fit value	320 TeV	880 TeV	700 TeV	700 TeV
68% range	(200, 400) TeV	(150, 950) TeV	(150, 1500) TeV	(150, 1500) TeV
$\tan\beta$: best-fit value	35	4.4	4.4	4.2
68% range	(28, 45)	(3, 50)	(3, 50)	(3, 50)
χ^2/d.o.f	33.7/27	36.4/27	36.4/27	36.4/27
χ^2 probability	17.5%	10.6%	10.6%	10.7%

5.4 Discovery prospects at the LHC and FCC-hh

As mentioned above, current LHC searches are not sensitive to the high-mass spectrum of mAMSB, even if the LSP is not the only component of CDM. However, simple extrapolation indicates that there are better prospects for future LHC searches with 300 or 3000 fb^{-1}. Searches for chargino tracks disappearing in the tracker, such as that performed by ATLAS [134] start to be sensitive with 300 fb^{-1}of data, and become much more sensitive with 3000 fb^{-1}, as shown in Fig. 20. We have obtained the projected contours for the 13 TeV LHC with 13,300 and 3000 fb^{-1}by rescaling the Run-1

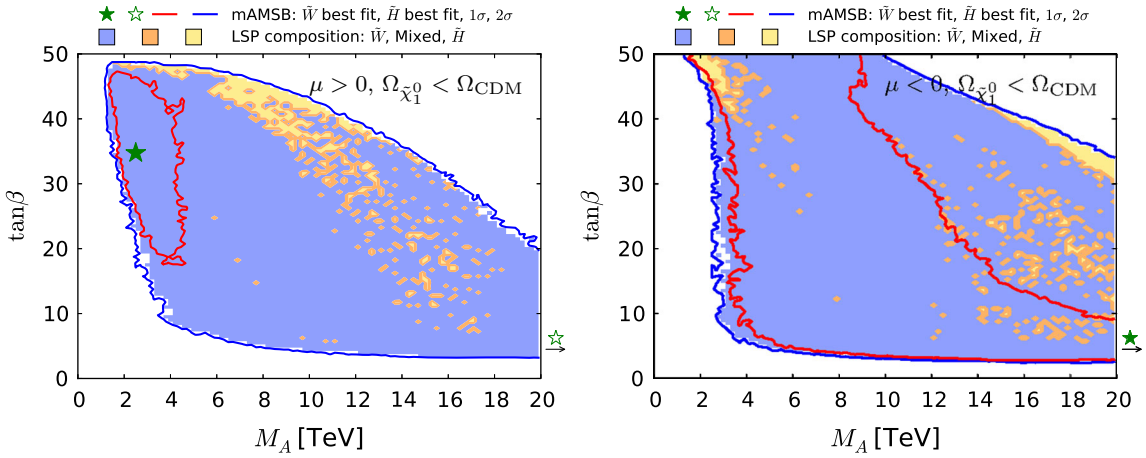

Fig. 14 The $(M_A, \tan\beta)$ planes for $\mu > 0$ (*left panel*) and for $\mu < 0$ (*right panel*), allowing the $\tilde{\chi}_1^0$ to contribute only part of the CDM density. The shadings are the same as in Fig. 4

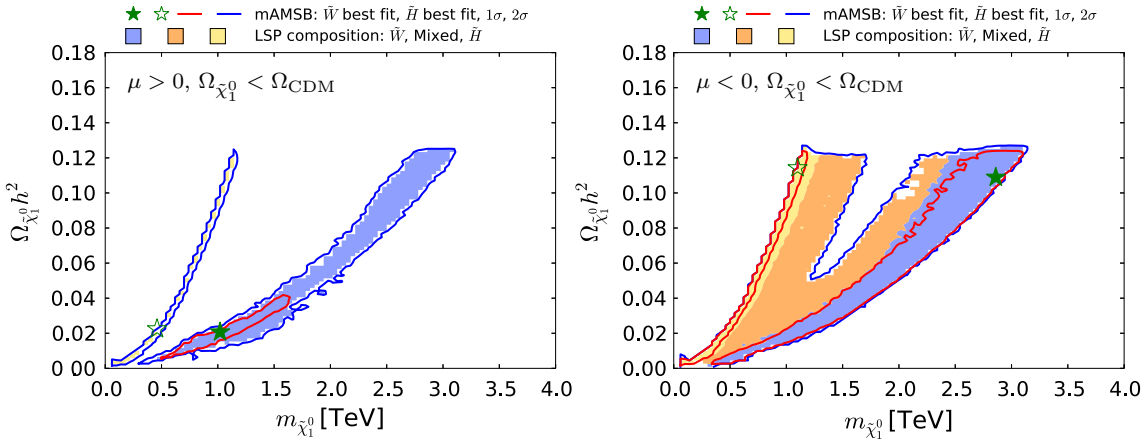

Fig. 15 The $(m_{\tilde{\chi}_1^0}, \Omega_{\tilde{\chi}_1^0} h^2)$ planes in the mAMSB for $\mu > 0$ (*left*) and $\mu < 0$ (*right*), allowing the $\tilde{\chi}_1^0$ to contribute only part of the CDM density. The *red (blue) contours* represent the 68% (95%) CL contours. The shadings are the same as in Fig. 4

sensitivity presented in [134]. In doing so, at a given lifetime we shift the Run-1 value of the 95% CL reach for the wino mass to the higher value at which the wino cross section times luminosity (13,300 and 3000 fb^{-1}) at the 13-TeV LHC coincides with the reach achieved during Run-1. This method is often used and is known to give a reasonable estimate [135]. We find that the disappearing-track search is more sensitive in the $\mu > 0$ case than in the $\mu < 0$ case because, in order to accommodate the reduced BR$(B_s \to \mu^+\mu^-)$, the wino-LSP solution is preferred over the Higgsino-LSP one.

The large mass reach of a 100 TeV pp collider would extend these sensitivities greatly. Reference [136,137] studied the capability of exploring the wino LSP scenario at a 100-TeV collider and found that the sensitivity reaches around $m_{\tilde{\chi}_1^\pm} \sim 3$ TeV at 3000 fb^{-1}. We therefore expect that at a 100-TeV collider with 3000 fb^{-1} almost the entire 68% CL region and a part of the 95% CL with $\tau_{\tilde{\chi}_1^\pm} > 0.1$ ns will be explored for $\mu > 0$ and < 0, respectively. If improvements on the detector and the analysis allow the sensitivity to be extended to $m_{\tilde{\chi}_1^\pm} \gtrsim 3$ TeV, the wino-like dark matter region in the scenario with $\Omega_{\tilde{\chi}_1^0} = \Omega_{\rm CDM}$ can also be probed.

Coloured sparticle searches that will become sensitive in future LHC runs are shown in Figs. 21, 22, and 23 in the $(m_{\tilde{g}}, m_{\tilde{q}_R})$, $(m_{\tilde{q}_R}, m_{\tilde{\chi}_1^0})$ and $(m_{\tilde{g}}, m_{\tilde{\chi}_1^0})$ planes, respectively, the latter being the most promising one. In these figures, exclusion contours from the Run-1 (orange) and the 13 TeV with 13 fb^{-1} (purple) data are taken from ATLAS analyses [138,139], respectively. Also superimposed are the projected 95% CL contours at the 14 TeV LHC with 300 (green dashed) and 3000 (green dotted) fb^{-1}estimated by ATLAS [140,141]. We also show, by grey dotted contours, the sensitivity at a 100 TeV collider with 3000 fb^{-1} taken from [142]. These contours assume simplified models with BR$(\tilde{q} \to q\tilde{\chi}_1^0) =$ BR$(\tilde{g} \to qq\tilde{\chi}_1^0) = 100\%$ for Figs. 22 and 23. For Fig. 21, in addition to these decays the heavier of the gluino and squark can also decay into the lighter one with an appropriate branching ratio. In Fig. 22 the projected LHC contours are estimated postulating $m_{\tilde{g}} = 4.5$

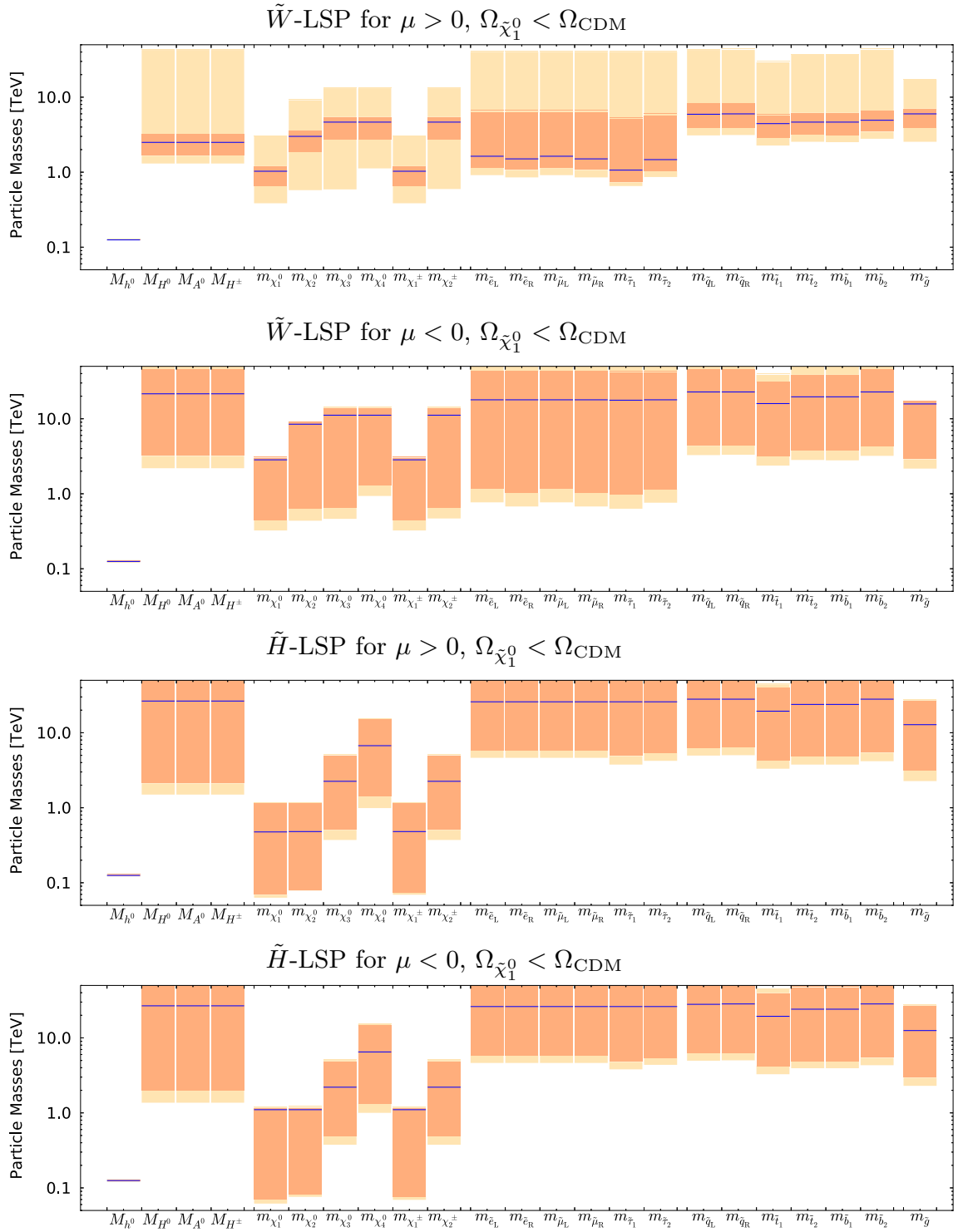

Fig. 16 The ranges of masses obtained for the wino-like LSP case with $\mu > 0$ (*top panel*) and $\mu < 0$ (*second panel*), and also for the Higgsino-like LSP case for $\mu > 0$ (*third panel*) and $\mu < 0$ (*bottom panel*), relaxing the assumption that the LSP contributes all the cold dark matter density. The one- and two-σ CL regions are shown in *dark and light orange* respectively, and the best-fit values are represented by *blue lines*

TeV, which is the right ball-park in our scenario. We see that with 3000 fb^{-1} the LHC could nip the tip of the 95% CL region in these planes, whereas with the same luminosity a 100-TeV collider would explore a sizeable region of the parameter space. In particular, the best-fit point and the 68% CL region are within this sensitivity for the $\mu > 0$ case.

Table 6 Ranges for the masses of the LSP $\tilde{\chi}_1^0$, the next-to-lightest neutralino $\tilde{\chi}_2^0$ and the mass splitting between the lighter chargino $\tilde{\chi}_1^\pm$ and the LSP and the corresponding lifetime of $\tilde{\chi}_1^\pm$ for the case in which the $\tilde{\chi}_1^0$ may accounts for only a fraction of the CDM density. Each parameter is shown for both the wino- and Higgsino-LSP scenarios as well as for the two signs of μ

Parameter	Wino-LSP		Higgsino	
	$\mu > 0$	$\mu < 0$	$\mu > 0$	$\mu < 0$
$m_{\tilde{\chi}_1^0}$	(0.7, 1.2) TeV	(0.5, 3.1) TeV	(0.07, 1.15) TeV	(0.07, 1.15) TeV
$m_{\tilde{\chi}_2^0}$	(1.9, 3.5) TeV	(0.6, 9.2) TeV	(0.08, 1.15) TeV	(0.08, 1.15) TeV
$m_{\tilde{\chi}_3^0}$	(2.8, 5.4) TeV	(0.6, 13.7) TeV	(0.5, 4.9) TeV	(0.5, 4.8) TeV
$m_{\tilde{\chi}_4^0}$	(2.8, 5.4) TeV	(1.3, 13.7) TeV	(1.4, 15.0) TeV	(1.3, 14.8) TeV
$m_{\tilde{g}}$	(3.9, 6.9) TeV	(2.9, 17.2) TeV	(3.1, 27) TeV	(3.0, 26) TeV
$m_{\tilde{\chi}_1^\pm} - m_{\tilde{\chi}_1^0}$	(0.16, 0.17) GeV	(0.16, 4.5) GeV	(0.7, 6.0) GeV	(1.3, 7.0) GeV
$\tau_{\tilde{\chi}_1^\pm}$	(0.15, 0.17) ns	(0.02, 0.17) ns	$<5.0 \times 10^{-3}$ ns	$<1.0 \times 10^{-3}$ ns

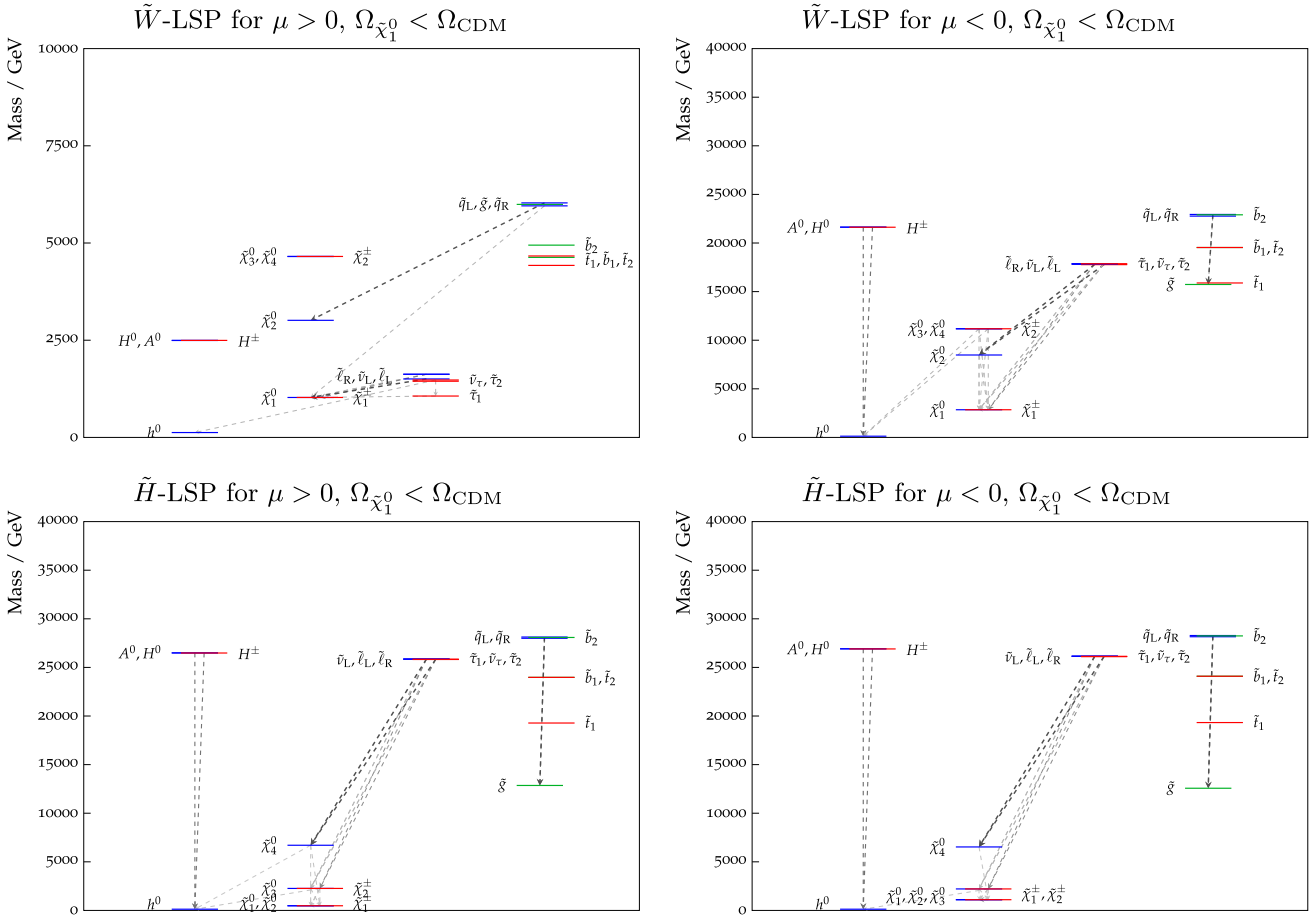

Fig. 17 The spectra of our best-fit points for $\mu > 0$ (*left panel*) and $\mu < 0$ (*right panel*), allowing the LSP to contribute only part of the cold dark matter density. Both the wino- (*upper*) and the Higgsino-like LSP (*lower*) best-fit points are shown. In each case, we also indicate all the decay modes with branching ratios (BRs) above 20%, with *darker shading* for larger BRs, and the *colours of the horizontal bars* reflect particles electric charges. The range of masses shown for the $\tilde{W}$-LSP $\mu > 0$ best-fit point (*top-left panel*) is smaller than the others, since its mass spectrum is considerably lighter

Allowing $\Omega_{\tilde{\chi}_1^0} < \Omega_{\rm CDM}$, we found in our sample very light winos as well as Higgsinos. If both of them are light but with a sufficiently large mass hierarchy between them, the LHC and a 100-TeV collider may be able to detect the production of a heavier state decaying subsequently into the lightest state by emitting the heavy bosons $W^\pm$, Z and h. In Fig. 24 we plot the current and future LHC reaches as well as the sensitivity expected at a 100-TeV collider with the same luminosity assumptions as in the previous figures. The current limit (purple) and projected sensitivity (green)

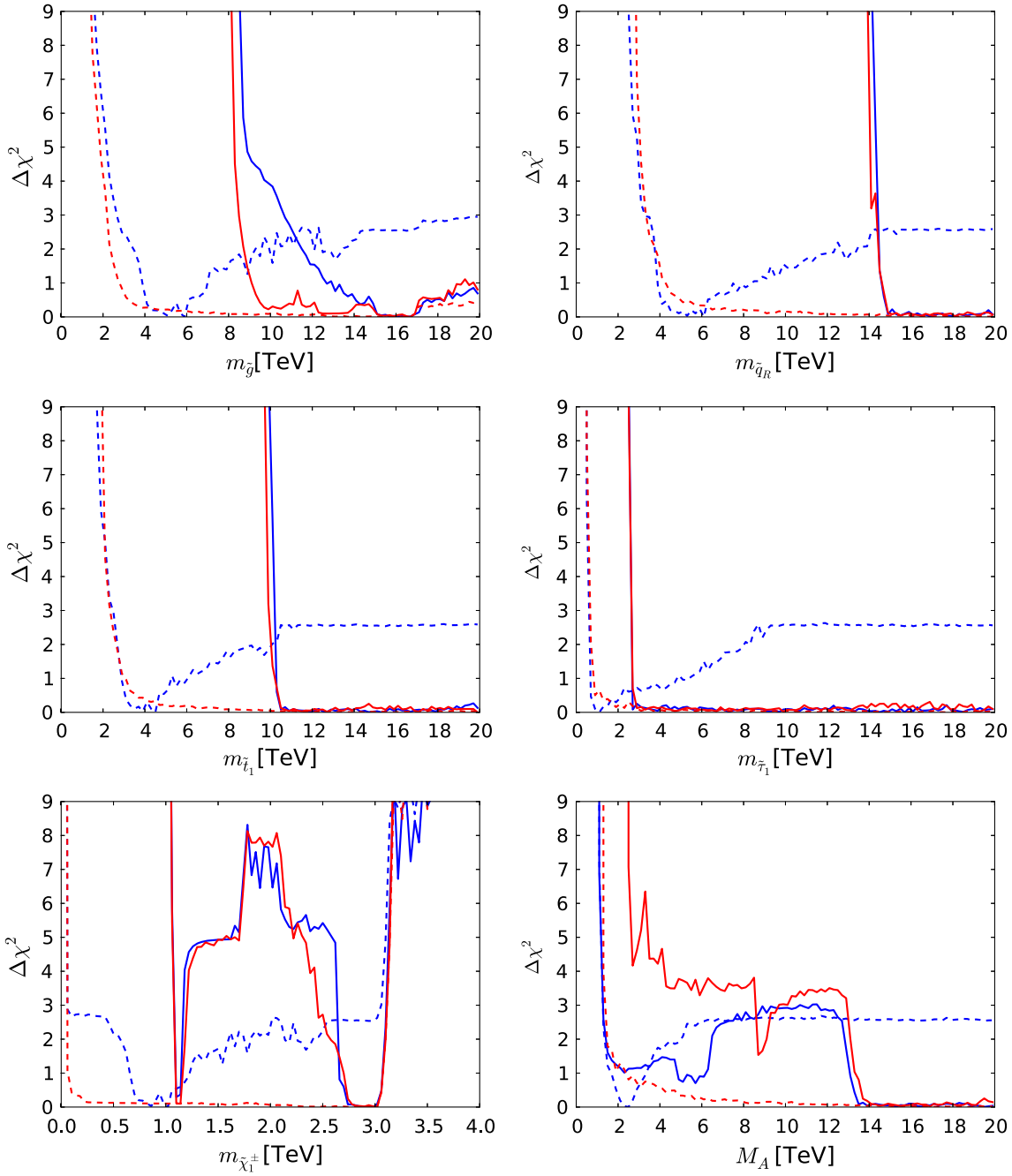

Fig. 18 The χ^2 likelihood functions for $m_{\tilde{g}}, m_{\tilde{q}}, m_{\tilde{t}_1}, m_{\tilde{\tau}_1}, m_{\tilde{\chi}_1^\pm}$ and M_A. We show curves with both $\Omega_{\tilde{\chi}_1^0} = \Omega_{\rm CDM}$ (*solid lines*), and with $\Omega_{\tilde{\chi}_1^0} \leq \Omega_{\rm CDM}$ (*dashed lines*), for both the $\mu > 0$ and $\mu < 0$ cases (*blue and red*, respectively)

at the LHC are estimated by CMS [143] and ATLAS [141] and assume wino-like chargino and neutralino production and a 100% rate for decay into the $W^\pm Z + \not{E}_T$ final state. As can be seen in Fig. 24, the region that can be explored is mainly the Higgsino-like LSP region, whereas we are interested in the wino-like chargino and neutralino production. However, unlike the simplified model assumption employed by ATLAS and CMS, the charged wino decays into neutral or charged Higgsinos emitting $W^\pm$, Z and h with 50, 25 and 25% branching ratio, respectively [144–146]. Similarly, the branching ratios of the neutral wino are 50, 25 and 25% for decays into $W^\pm$, Z and h, respectively. In total, only 25% of the associated charged and neutral wino production events contribute to the $W^\pm Z + \not{E}_T$ channel. The LHC contours shown in Fig. 24 should be considered with this caveat. Also shown by the grey dotted line is the sensitivity expected at a

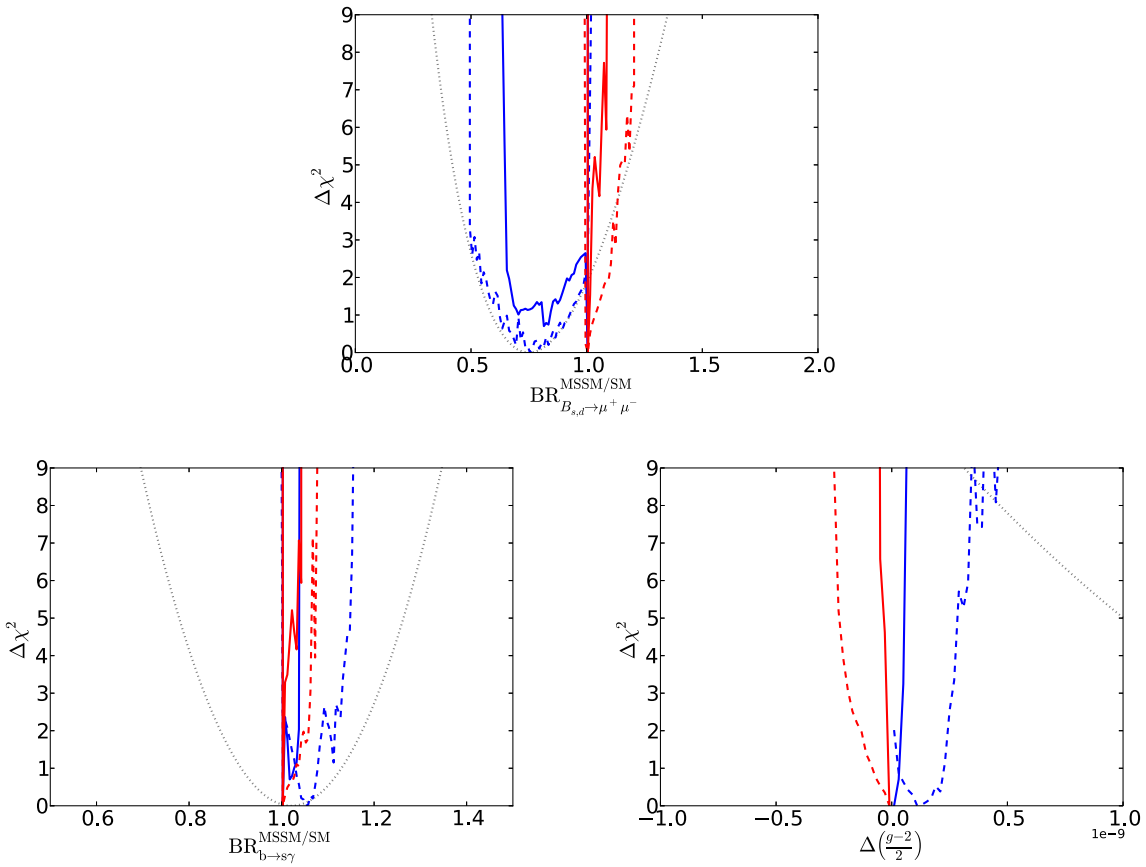

Fig. 19 The χ^2 likelihood functions for the ratios of $\mathrm{BR}(B_{s,d} \to \mu^+\mu^-)$, $\mathrm{BR}(b \to s\gamma)$ to their SM values, and for the contribution to $(g-2)_\mu/2$. We show curves with both $\Omega_{\tilde{\chi}_1^0} = \Omega_{\mathrm{CDM}}$ (*solid lines*), and with $\Omega_{\tilde{\chi}_1^0} \leq \Omega_{\mathrm{CDM}}$ (*dashed lines*), as well as both the $\mu > 0$ and $\mu < 0$ cases (*blue and red*, respectively). The *dotted lines* represent the current experimental measurements of these observables

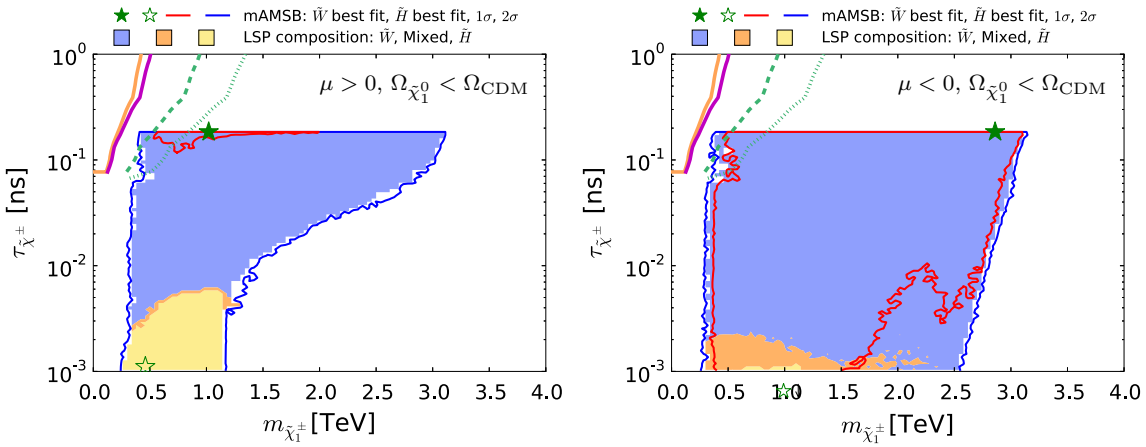

Fig. 20 The region of the $(m_{\tilde{\chi}_1^\pm}, \tau_{\tilde{\chi}_1^\pm})$ plane allowed in the $\Omega_{\tilde{\chi}_1^0} \leq \Omega_{\mathrm{CDM}}$ case for $\mu > 0$ (*left*) and $\mu < 0$ (*right*). The *orange solid line* represents the limit from the ATLAS 8-TeV search for disappearing tracks [134]. The *magenta solid, green dashed and green dotted lines* represents the projection of this limit to 13- TeV data with 13, 300 and 3000 fb^{-1}, respectively. The shadings are the same as in Fig. 4

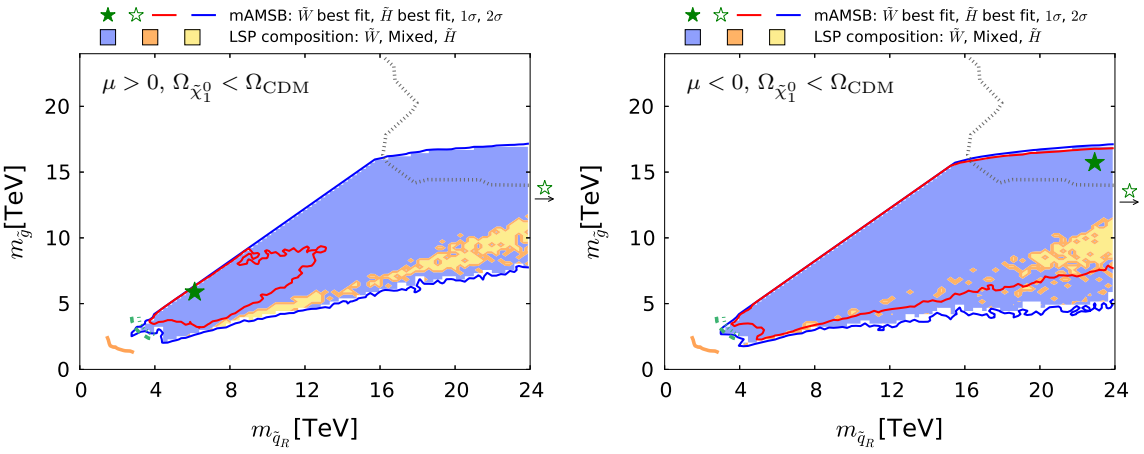

Fig. 21 The region of the $(m_{\tilde{q}_R}, m_{\tilde{g}})$ plane allowed in the $\Omega_{\tilde{\chi}_1^0} \leq \Omega_{\rm CDM}$ case for $\mu > 0$ (*left*) and $\mu < 0$ (*right*). The *orange solid line* represents the LHC 8-TeV 95% CL exclusion [138]. The *green dashed and dotted lines* show the projection estimated by ATLAS [140] for 14-TeV data with 300 and 3000 fb^{-1}, respectively. The *grey dotted line* is the 95% CL sensitivity expected at a 100 TeV pp collider with a 3000 fb^{-1} integrated luminosity obtained from [142]. All contours assume massless $\tilde{\chi}_1^0$. The shadings are the same as in Fig. 4

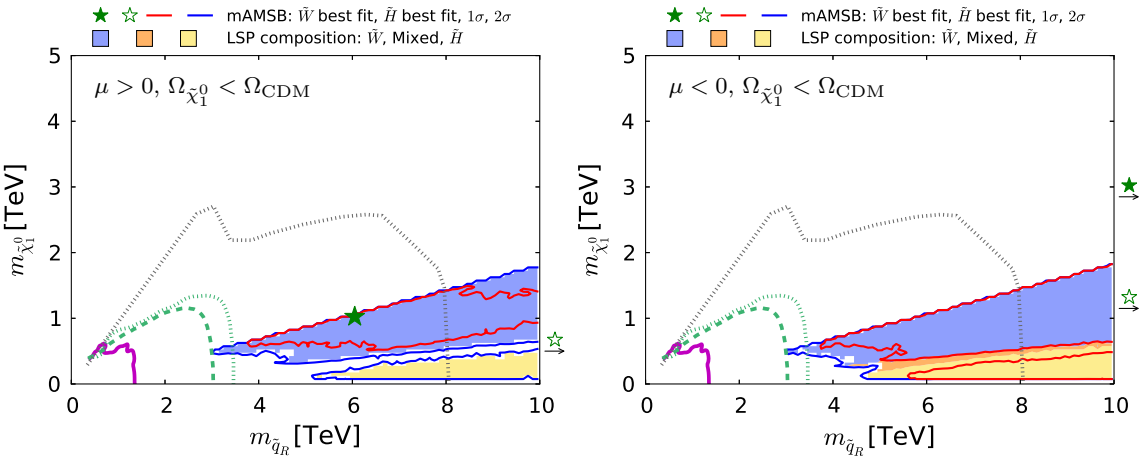

Fig. 22 The region of the $(m_{\tilde{q}_R}, m_{\tilde{\chi}_1^0})$ plane allowed in the $\Omega_{\tilde{\chi}_1^0} \leq \Omega_{\rm CDM}$ case for $\mu > 0$ (*left*) and $\mu < 0$ (*right*). The *purple solid line* represents the ATLAS 13-TeV 95% CL exclusion using 13 fb^{-1} of data [139]. The *green dashed and dotted lines* show the projected 95% CL sensitivity estimated by ATLAS [141] for 14-TeV data with integrated luminosities of 300 and 3000 fb^{-1}, respectively. The *grey dotted line* is the 95% CL sensitivity expected at a 100 TeV pp collider with a 3000 fb^{-1} integrated luminosity obtained from [142]. All contours assume a simplified model with 100% BR for $\tilde{q} \to q\tilde{\chi}_1^0$. The current limit and 100 TeV projection assumes decoupled gluino, while the projection to the higher luminosity LHC assumes a 4.5-TeV gluino. The shadings are the same as in Fig. 4

100-TeV collider with 3000 fb^{-1} luminosity studied in [144] (see also [146]) assuming a Higgsino-like LSP and wino-like chargino and neutralino production, taking into account the correct branching ratios mentioned above. As can be seen, a 100-TeV collider is sensitive up to $m_{\tilde{\chi}_3^0} \sim 2$ TeV, and a large part of the 95% CL region would be within reach, and also a substantial portion of the 68% CL region if $\mu < 0$, though not the best-fit point for either sign of μ.

Finally, in Fig. 25 we show the $(m_{\tilde{g}}, m_{\tilde{q}_R})$ plane for the scenario with $\Omega_{\tilde{\chi}_1^0} = \Omega_{\rm CDM}$. We found that a small part of the wino-like dark matter region and a good amount of the Higgsino-like dark matter region are within the 95% CL sensitivity region at a 100-TeV collider with 3000 fb^{-1}. In particular, the sensitivity contour reaches the best-fit point for the $\mu > 0$ case.

5.5 Prospects for direct detection of dark matter

While the heavy spectra of mAMSB models may lie beyond the reach of the LHC constraints, future direct DM search experiments may be capable of detecting the interaction of a mAMSB neutralino, even if it does not provide all the CDM density [147–150]. Figure 26 displays the cross section for spin-independent scattering on a proton, $\sigma_p^{\rm SI}$, versus the neu-

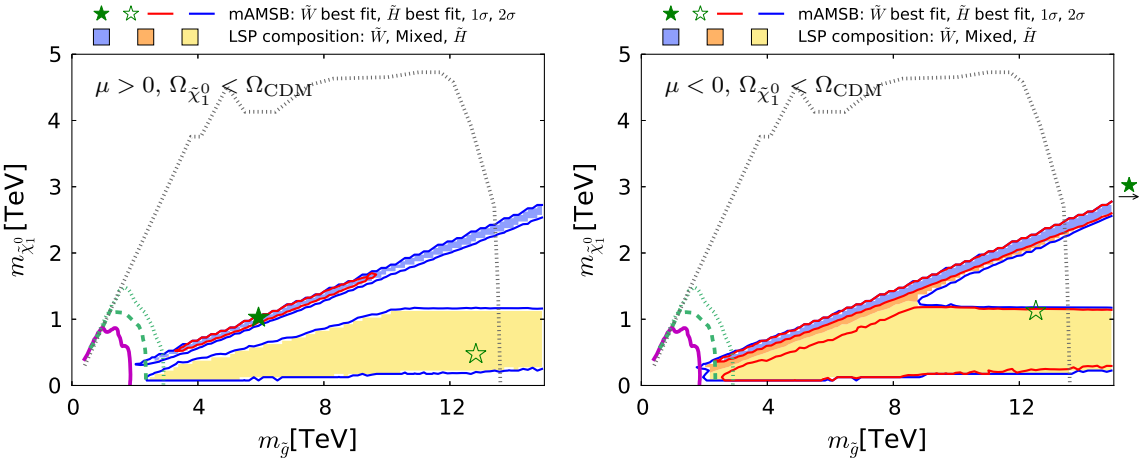

Fig. 23 The region of the $(m_{\tilde{g}}, m_{\tilde{\chi}_1^0})$ plane allowed in the $\Omega_{\tilde{\chi}_1^0} \leq \Omega_{\rm CDM}$ case for $\mu > 0$ (*left*) and $\mu < 0$ (*right*). The *purple solid line* represents the ATLAS 13-TeV 95% CL exclusion with the data with 13 fb^{-1} [139]. The *green dashed and dotted lines* show the projected 95% CL sensitivity estimated by ATLAS [141] for 14-TeV data with integrated luminosities of 300 and 3000 fb^{-1}, respectively. The *grey dotted line* is the 95% CL sensitivity expected at a 100 TeV pp collider with a 3000 fb^{-1} integrated luminosity obtained from [142]. All contours assume a simplified model with 100% BR for $\tilde{g} \to qq\tilde{\chi}_1^0$. The shadings are the same as in Fig. 4

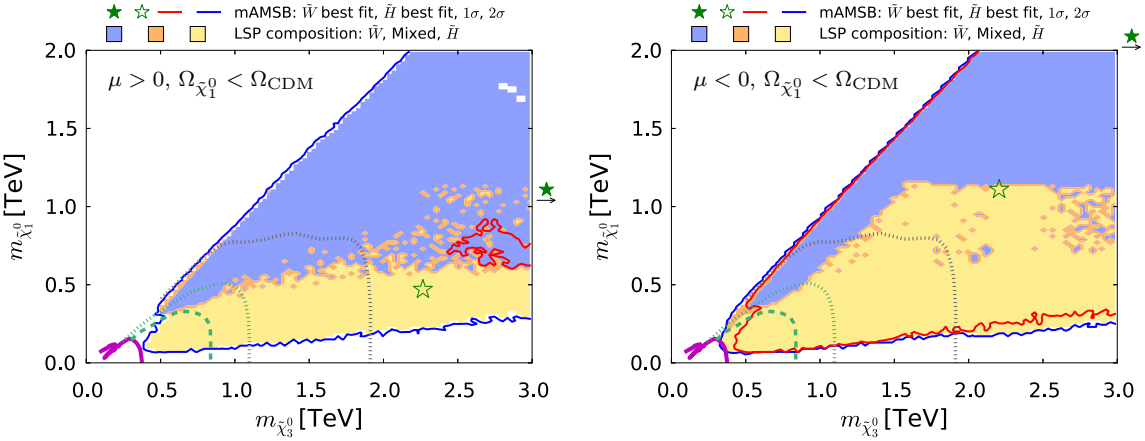

Fig. 24 The region of the $(m_{\tilde{\chi}_3^0}, m_{\tilde{\chi}_1^0})$ plane allowed in the $\Omega_{\tilde{\chi}_1^0} \leq \Omega_{\rm CDM}$ case for $\mu > 0$ (*left*) and $\mu < 0$ (*right*). The *purple solid line* represents the CMS 13-TeV 95% CL exclusion [143] assuming a simplified model with wino-like chargino and neutralino production and 100% BR for the $W^{\pm}Z + \not{E}_T$ final state. The *green dashed (dotted) line* shows the projected sensitivity for 14-TeV data with an integrated luminosity of 300 fb^{-1} (3000 fb^{-1}) estimated by ATLAS [141]. The *grey dotted line* is the 95% CL sensitivity expected at a 100 TeV pp collider with a 3000 fb^{-1} integrated luminosity obtained from [144]. The shadings are the same as in Fig. 4

tralino mass. As previously, the left plane is for $\mu > 0$, the right plane is for $\mu < 0$, the 1 and 2σ CL contours are shown as red and blue lines, and the wino- and Higgsino-LSP regions are shaded in pale blue and yellow. The pale-green-shaded region represents the range of $\sigma_p^{\rm SI}$ excluded at the 95% CL by our combination of the latest PandaX and LUX results [151,152], while the purple and blue lines show the prospective sensitivities of the LUX-Zeplin (LZ), XENON1T and XENONnT experiments [153–155]. Also shown, as a dashed orange line, is the neutrino 'floor', below which astrophysical neutrino backgrounds would dominate any DM signal [156] (grey region). The mAMSB region allowed at the 2σ level includes points where $\sigma_p^{\rm SI}$ is nominally larger than that excluded by LUX and PandaX at the 95% CL, which become allowed when the large theoretical uncertainty in $\sigma_p^{\rm SI}$ is taken into account.

This uncertainty stems largely from the uncertainty in the strangeness contribution to the nucleon, which receives contributions from two sources. The strange scalar density can be written as $y = 1 - \sigma_0/\Sigma_{\pi N}$ where σ_0 is the change in the nucleon mass due to the non-zero u, d quark masses, and is estimated from octet baryon mass differences to be $\sigma_0 = 36 \pm 7$ MeV [157–159]. This is the dominant source of error in the computed cross section. In addition, the π-

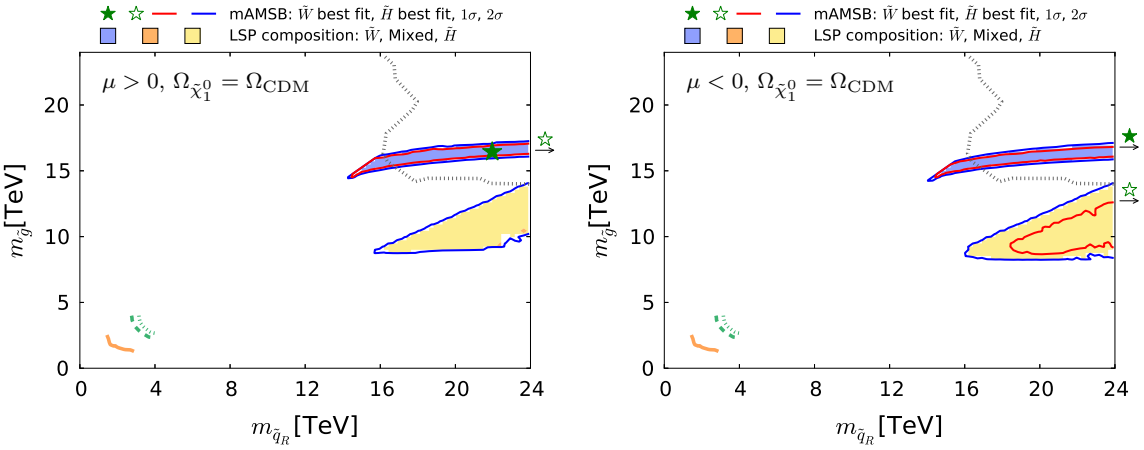

Fig. 25 The region of the $(m_{\tilde{q}_R}, m_{\tilde{g}})$ plane allowed in the $\Omega_{\tilde{\chi}_1^0} = \Omega_{\rm CDM}$ case for $\mu > 0$ (*left*) and $\mu < 0$ (*right*). The *orange solid line* represents the LHC 8-TeV 95% CL exclusion [138]. The *green dashed and dotted lines* show the projection estimated by ATLAS [140] for 14-TeV data with 300 and 3000 fb^{-1}, respectively. The *grey dotted line* is the 95% CL sensitivity expected at a 100 TeV pp collider with a 3000 fb^{-1} integrated luminosity obtained from [142]. All contours assume massless $\tilde{\chi}_1^0$. The shadings are the same as in Fig. 4

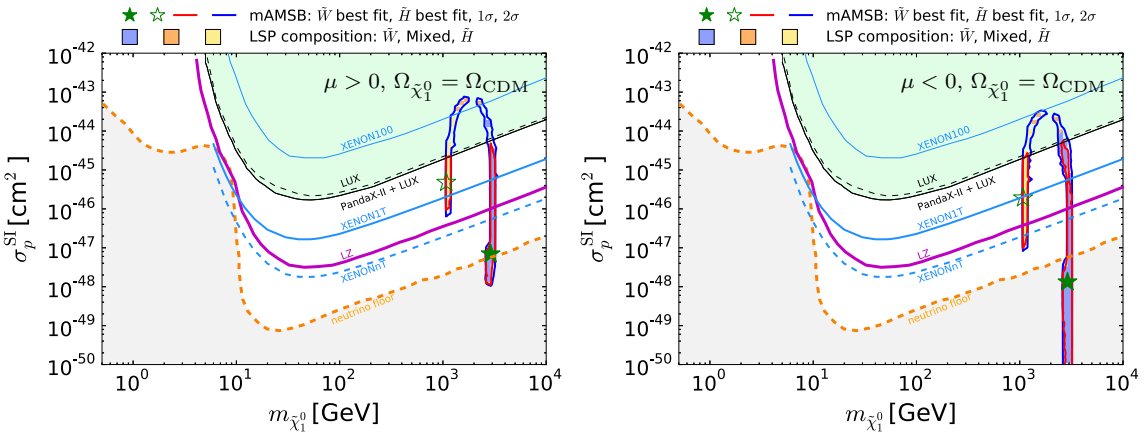

Fig. 26 The $(m_{\tilde{\chi}_1^0}, \sigma_p^{\rm SI})$ planes in the mAMSB for $\mu > 0$ (*left*) and $\mu < 0$ (*right*) in the case when the LSP accounts for the whole DM density. The *red and blue solid lines* are the 1 and 2 σ CL contours, and the *solid purple and blue lines* show the projected 95% exclusion sensitivities of the LUX-Zeplin (LZ) [153] and XENON1T/nT experiments [154,155], respectively. The *green line and shaded region* show the combined limit from the LUX and PandaX experiments [151,152], and the *dashed orange line* shows the astrophysical neutrino 'floor' [156], below which astrophysical neutrino backgrounds dominate (*grey region*). The *blue, orange and yellow shadings* are the same as in Fig. 4

nucleon Σ term is taken as 50 ± 8 MeV. Another non-negligible source of error comes from the uncertainty in quark masses. The resulting 68% CL uncertainty in the calculated value of $\sigma_p^{\rm SI}$ is more than 50%.

However, the current data already put pressure on the mAMSB when $\mu > 0$, in both the wino- and Higgsino-like LSP cases, corresponding to the left and right vertical strips in Fig. 26.[11] The Higgsino-like $\tilde{\chi}_1^0$ with this sign of μ could be explored completely with the prospective LZ sensitivity, while the wino-like LSP may have $\sigma_p^{\rm SI}$ below the neutrino 'floor'. The wino-like LSP region lying below the LZ sensitivity could be partly accessible to a 20-tonne DM experiment such as Darwin [160]. When $\mu < 0$, $\sigma_p^{\rm SI}$ may be lower than for positive μ, possibly lying below the LZ sensitivity in the Higgsino case and far below the neutrino 'floor' in the wino case.

Figure 27 extends the analysis to the case in which the LSP is allowed to contribute only a fraction of the CDM density. In this case we weight the model value $\sigma_p^{\rm SI}$ by the ratio $\Omega_{\tilde{\chi}_1^0}/\Omega_{\rm CDM}$, since this would be the fraction of the galactic halo provided by the LSP in this case. There are still reasonably good prospects for future DM direct detection experiments when $\mu > 0$, with only a small fraction of the parameter space lying below the neutrino 'floor'. However,

[11] The arches between them, where the LSP has a mixed wino/Higgsino composition, are under severe pressure from LUX and PandaX.

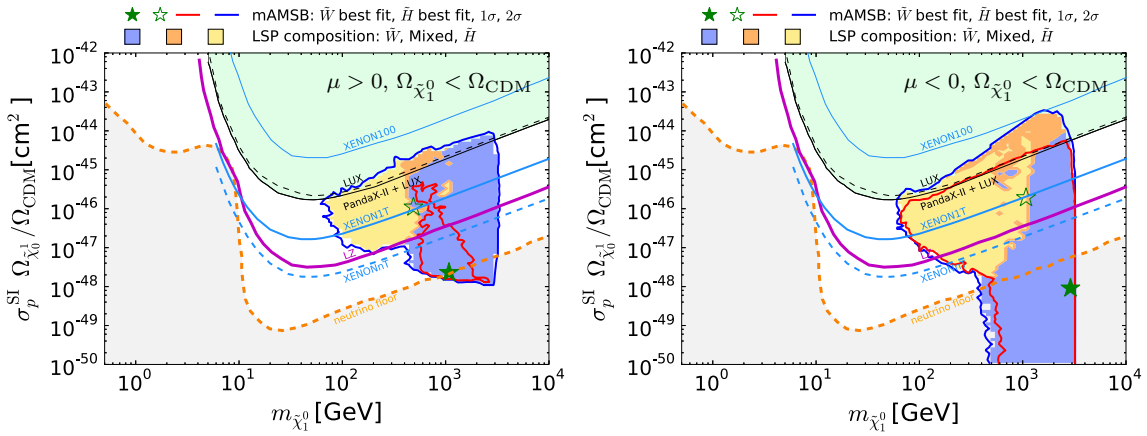

Fig. 27 The $(m_{\tilde{\chi}_1^0}, \sigma_p^{\rm SI})$ planes in the mAMSB for $\mu > 0$ (*left*) and $\mu < 0$ (*right*) in the case when the LSP only accounts for a fraction of the CDM density. The legends, line styles and shadings are the same as in Fig. 26

when $\mu < 0$ $\sigma_p^{\rm SI}$ may fall considerably below the 'floor', because of cancellations [161–165] in the scattering matrix element.

6 Summary

Using the `MasterCode` framework, we have constructed in this paper a global likelihood function for the minimal AMSB model and explored the constraints imposed by the available data on flavour, electroweak and Higgs observables, as well as by LHC searches for gluinos via $\not{E}_T$ signatures. We have also included the constraint imposed by the cosmological cold dark matter density, which we interpret as either a measurement or an upper limit on the relic LSP density, and searches for dark matter scattering.

In the all-CDM case, we find that the spectrum is relatively heavy, with strongly interacting sparticles weighing $\gtrsim$10 TeV, but much smaller masses are possible if the LSP contributes only a fraction of the overall CDM density. In the all-CDM case, the LSP composition may be either wino- or Higgsino-like with almost equal likelihood, weighing $\sim$3 TeV and $\sim$1 TeV, respectively. On the other hand, in the part-CDM case much lighter LSP masses are allowed at the 68% CL, as are intermediate LSP masses.

Because of the high masses in the all-CDM case, the prospects for discovering sparticles at the LHC are small, and there are limited prospects for observing significant deviations for the SM predictions for flavour observables. However, in the part-CDM case some sparticles may well be within reach of the LHC, and there are more interesting possibilities for observing mAMSB effects on flavour observables, e.g., BR$(B_{s,d} \to \mu^+\mu^-)$. In both cases, wide ranges of dark matter scattering cross sections, $\sigma_p^{\rm SI}$ are allowed: $\sigma_p^{\rm SI}$ may be very close to the upper limits established recently by the PandaX and LUX experiments, or it may be within reach of the planned LUX-Zeplin experiment, or it may even be far below the neutrino 'floor'.

The mAMSB scenario discussed in this paper clearly presents different challenges from the models with GUT-scale unification of (at least some of) the soft SUSY-breaking parameters that we have studied previously [1–5,7,8], and it does not share the flexibility of pMSSM models [6,166]. As such, the mAMSB serves as a useful reminder that SUSY phenomenology may differ significantly from what is preferred in these other scenarios.

Acknowledgements The work of E.B. and G.W. is supported in part by the Collaborative Research Center SFB676 of the DFG, "Particles, Strings and the early Universe", and by the European Commission through the "HiggsTools" Initial Training Network PITN-GA-2012-316704. The work of R.C. is supported in part by the National Science Foundation under Grant No. PHY-1151640 at the University of Illinois Chicago and in part by Fermilab, operated by Fermi Research Alliance, LLC under Contract No. De-AC02-07CH11359 with the United States Department of Energy. This work of M.J.D. is supported in part by the Australian Research Council. The work of J.E. is supported in part by STFC (UK) via the research Grant ST/L000326/1, and the work of H.F. is also supported in part by STFC (UK). The work of S.H. is supported in part by CICYT (Grant FPA 2013-40715-P) and by the Spanish MICINN's Consolider-Ingenio 2010 Program under Grant MultiDark CSD2009-00064. The work of D.M.-S. is supported by the European Research Council via Grant BSMFLEET 639068. The work of F.L. is supported by World Premier International Research Center Initiative (WPI), MEXT, Japan. The work of K.A.O. is supported in part by DOE Grant DE-SC0011842 at the University of Minnesota. KS is supported by STFC through the IPPP grant. The work of K.S. is partially supported by the National Science Centre, Poland, under research Grants DEC-2014/15/B/ST2/02157 and DEC-2015/18/M/ST2/00054.

References

1. O. Buchmueller et al., Eur. Phys. J. C **72**, 1878 (2012). arXiv:1110.3568 [hep-ph]
2. O. Buchmueller et al., Eur. Phys. J. C **72**, 2243 (2012). arXiv:1207.7315
3. O. Buchmueller et al., Eur. Phys. J. C **74**, 2809 (2014). arXiv:1312.5233 [hep-ph]
4. O. Buchmueller et al., Eur. Phys. J. C **74**, 2922 (2014). arXiv:1312.5250 [hep-ph]
5. O. Buchmueller et al., Eur. Phys. J. C **74**(12), 3212 (2014). arXiv:1508.01173 [hep-ph]
6. K.J. de Vries et al., Eur. Phys. J. C **75**(9), 422 (2015). arXiv:1504.03260 [hep-ph]
7. E.A. Bagnaschi et al., Eur. Phys. J. C **75**, 500 (2015). arXiv:1508.01173 [hep-ph]
8. E. Bagnaschi et al., arXiv:1610.10084 [hep-ph]
9. M. Drees, M.M. Nojiri, Phys. Rev. D **47**, 376 (1993). arXiv:hep-ph/9207234
10. G.L. Kane, C.F. Kolda, L. Roszkowski, J.D. Wells, Phys. Rev. D **49**, 6173 (1994). arXiv:hep-ph/9312272
11. H. Baer, M. Brhlik, Phys. Rev. D **53**, 597 (1996). arXiv:hep-ph/9508321
12. J.R. Ellis, T. Falk, K.A. Olive, M. Schmitt, Phys. Lett. B **388**, 97 (1996). arXiv:hep-ph/9607292
13. J.R. Ellis, T. Falk, K.A. Olive, M. Schmitt, Phys. Lett. B **413**, 355 (1997). arXiv:hep-ph/9705444
14. H. Baer, M. Brhlik, Phys. Rev. D **57**, 567 (1998). arXiv:hep-ph/9706509
15. J.R. Ellis, T. Falk, G. Ganis, K.A. Olive, M. Schmitt, Phys. Rev. D **58**, 095002 (1998). arXiv:hep-ph/9801445
16. V.D. Barger, C. Kao, Phys. Rev. D **57**, 3131 (1998). arXiv:hep-ph/9704403
17. J.R. Ellis, T. Falk, G. Ganis, K.A. Olive, Phys. Rev. D **62**, 075010 (2000). arXiv:hep-ph/0004169
18. H. Baer, M. Brhlik, M.A. Diaz, J. Ferrandis, P. Mercadante, P. Quintana, X. Tata, Phys. Rev. D **63**, 015007 (2001). arXiv:hep-ph/0005027
19. J.R. Ellis, T. Falk, G. Ganis, K.A. Olive, M. Srednicki, Phys. Lett. B **510**, 236 (2001). arXiv:hep-ph/0102098
20. L. Roszkowski, R. Ruiz de Austri, T. Nihei, JHEP **0108**, 024 (2001). arXiv:hep-ph/0106334
21. A. Djouadi, M. Drees, J.L. Kneur, JHEP **0108**, 055 (2001). arXiv:hep-ph/0107316
22. U. Chattopadhyay, A. Corsetti, P. Nath, Phys. Rev. D **66**, 035003 (2002). arXiv:hep-ph/0201001
23. J.R. Ellis, K.A. Olive, Y. Santoso, New J. Phys. **4**, 32 (2002). arXiv:hep-ph/0202110
24. H. Baer, C. Balazs, A. Belyaev, J.K. Mizukoshi, X. Tata, Y. Wang, JHEP **0207**, 050 (2002). arXiv:hep-ph/0205325
25. R. Arnowitt, B. Dutta, arXiv:hep-ph/0211417
26. H. Baer, A. Mustafayev, S. Profumo, A. Belyaev, X. Tata, Phys. Rev. D **71**, 095008 (2005). arXiv:hep-ph/0412059
27. H. Baer, A. Mustafayev, S. Profumo, A. Belyaev, X. Tata, JHEP **0507**, 065 (2005). arXiv:hep-ph/0504001
28. J.R. Ellis, K.A. Olive, P. Sandick, Phys. Rev. D **78**, 075012 (2008). arXiv:0805.2343 [hep-ph]
29. J. Ellis, F. Luo, K.A. Olive, P. Sandick, Eur. Phys. J. C **73**, 2403 (2013). arXiv:1212.4476 [hep-ph]
30. J. Ellis, J.L. Evans, F. Luo, N. Nagata, K.A. Olive, P. Sandick, Eur. Phys. J. C **76**(1), 8 (2016). arXiv:1509.08838 [hep-ph]
31. J. Ellis, K. Olive, Y. Santoso, Phys. Lett. B **539**, 107 (2002). arXiv:hep-ph/0204192
32. J.R. Ellis, T. Falk, K.A. Olive, Y. Santoso, Nucl. Phys. B **652**, 259 (2003). arXiv:hep-ph/0210205
33. C.F. Berger, J.S. Gainer, J.L. Hewett, T.G. Rizzo, JHEP **0902**, 023 (2009). arXiv:0812.0980 [hep-ph]
34. S.S. AbdusSalam, B.C. Allanach, F. Quevedo, F. Feroz, M. Hobson, Phys. Rev. D **81**, 095012 (2010). arXiv:0904.2548 [hep-ph]
35. J.A. Conley, J.S. Gainer, J.L. Hewett, M.P. Le, T.G. Rizzo, Eur. Phys. J. C **71**, 1697 (2011). arXiv:1009.2539 [hep-ph]
36. J.A. Conley, J.S. Gainer, J.L. Hewett, M.P. Le, T.G. Rizzo, arXiv:1103.1697 [hep-ph]
37. B.C. Allanach, A.J. Barr, A. Dafinca, C. Gwenlan, JHEP **1107**, 104 (2011). arXiv:1105.1024 [hep-ph]
38. S.S. AbdusSalam et al., Eur. Phys. J. C **71**, 1835 (2011). arXiv:1109.3859 [hep-ph]
39. S. Sekmen, S. Kraml, J. Lykken, F. Moortgat, S. Padhi, L. Pape, M. Pierini, H.B. Prosper et al., JHEP **1202**, 075 (2012). arXiv:1109.5119 [hep-ph]
40. A. Arbey, M. Battaglia, F. Mahmoudi, Eur. Phys. J. C **72**, 1847 (2012). arXiv:1110.3726 [hep-ph]
41. A. Arbey, M. Battaglia, A. Djouadi, F. Mahmoudi, Phys. Lett. B **720**, 153 (2013). arXiv:1211.4004 [hep-ph]
42. M.W. Cahill-Rowley, J.L. Hewett, A. Ismail, T.G. Rizzo, Phys. Rev. D **88** (2013) 3, 035002. arXiv:1211.1981 [hep-ph]
43. C. Strege, G. Bertone, G.J. Besjes, S. Caron, R. Ruiz de Austri, A. Strubig, R. Trotta, JHEP **1409**, 081 (2014). arXiv:1405.0622 [hep-ph]
44. M. Cahill-Rowley, J.L. Hewett, A. Ismail, T.G. Rizzo, Phys. Rev. D **91**(5), 055002 (2015). arXiv:1407.4130 [hep-ph]
45. L. Roszkowski, E.M. Sessolo, A.J. Williams, JHEP **1502**, 014 (2015). arXiv:1411.5214 [hep-ph]
46. M.E. Cabrera-Catalan, S. Ando, C. Weniger, F. Zandanel, Phys. Rev. D **92**,(3), 035018 (2015). arXiv:1503.00599 [hep-ph]
47. J. Chakrabortty, A. Choudhury, S. Mondal, JHEP **1507**, 038 (2015). arXiv:1503.08703 [hep-ph]
48. M. Cannoni, J. Ellis, M.E. Gmez, S. Lola, R. Ruiz de Austri, JCAP **1603**(03), 041 (2016). arXiv:1511.06205 [hep-ph]
49. H. Goldberg, Phys. Rev. Lett. **50**, 1419 (1983)
50. J. Ellis, J. Hagelin, D. Nanopoulos, K. Olive, M. Srednicki, Nucl. Phys. B **238**, 453 (1984)
51. M. Dine, D. MacIntire, Phys. Rev. D **46**, 2594 (1992). arXiv:hep-ph/9205227
52. L. Randall, R. Sundrum, Nucl. Phys. B **557**, 79 (1999). arXiv:hep-th/9810155
53. G.F. Giudice, M.A. Luty, H. Murayama, R. Rattazzi, JHEP **9812**, 027 (1998). arXiv:hep-ph/9810442
54. A. Pomarol, R. Rattazzi, JHEP **9905**, 013 (1999). arXiv:hep-ph/9903448
55. J.A. Bagger, T. Moroi, E. Poppitz, JHEP **0004**, 009 (2000). arXiv:hep-th/9911029
56. P. Binetruy, M.K. Gaillard, B.D. Nelson, Nucl. Phys. B **604**, 32 (2001). arXiv:hep-ph/0011081
57. T. Gherghetta, G. Giudice, J. Wells, Nucl. Phys. B **559**, 27 (1999). arXiv:hep-ph/9904378
58. E. Katz, Y. Shadmi, Y. Shirman, JHEP **9908**, 015 (1999). arXiv:hep-ph/9906296
59. Z. Chacko, M.A. Luty, I. Maksymyk, E. Ponton, JHEP **0004**, 001 (2000). arXiv:hep-ph/9905390
60. J.L. Feng, T. Moroi, Phys. Rev. D **61**, 095004 (2000). arXiv:hep-ph/9907319
61. G.D. Kribs, Phys. Rev. D **62**, 015008 (2000). arXiv:hep-ph/9909376
62. U. Chattopadhyay, D.K. Ghosh, S. Roy, Phys. Rev. D **62**, 115001 (2000). arXiv:hep-ph/0006049
63. I. Jack, D.R.T. Jones, Phys. Lett. B **491**, 151 (2000). arXiv:hep-ph/0006116
64. H. Baer, J.K. Mizukoshi, X. Tata, Phys. Lett. B **488**, 367 (2000). arXiv:hep-ph/0007073

65. A. Datta, A. Kundu, A. Samanta, Phys. Rev. D **64**, 095016 (2001). arXiv:hep-ph/0101034
66. H. Baer, R. Dermisek, S. Rajagopalan, H. Summy, JCAP **1007**, 014 (2010). arXiv:1004.3297 [hep-ph]
67. A. Arbey, A. Deandrea, A. Tarhini, JHEP **1105**, 078 (2011). arXiv:1103.3244 [hep-ph]
68. B.C. Allanach, T.J. Khoo, K. Sakurai, JHEP **1111**, 132 (2011). arXiv:1110.1119 [hep-ph]
69. A. Arbey, A. Deandrea, F. Mahmoudi, A. Tarhini, Phys. Rev. D **87**(11), 115020 (2013). arXiv:1304.0381 [hep-ph]
70. M. Ibe, T. Moroi, T.T. Yanagida, Phys. Lett. B **644**, 355 (2007). arXiv:hep-ph/0610277
71. J.L. Evans, M. Ibe, K.A. Olive, T.T. Yanagida, Eur. Phys. J. C **73**, 2468 (2013). arXiv:1302.5346 [hep-ph]
72. J.L. Evans, N. Nagata, K.A. Olive, Phys. Rev. D **91**, 055027 (2015). arXiv:1502.00034 [hep-ph]
73. P.A.R. Ade et al., Planck Collaboration. Astron. Astrophys. **594**, A13 (2016). arXiv:1502.01589 [astro-ph.CO]
74. J. Hisano, S. Matsumoto, M. Nagai, O. Saito, M. Senami, Phys. Lett. B **646**, 34 (2007). arXiv:hep-ph/0610249
75. M. Cirelli, A. Strumia, M. Tamburini, Nucl. Phys. B **787**, 152 (2007). arXiv:0706.4071 [hep-ph]
76. A. Hryczuk, R. Iengo, P. Ullio, JHEP **1103**, 069 (2011). arXiv:1010.2172 [hep-ph]
77. M. Beneke, A. Bharucha, F. Dighera, C. Hellmann, A. Hryczuk, S. Recksiegel, P. Ruiz-Femenia, JHEP **1603**, 119 (2016). arXiv:1601.04718 [hep-ph]
78. A. Sommerfeld, Ann. Phys. **403**, 257 (1931)
79. G. Aad et al. [ATLAS and CMS Collaborations], Phys. Rev. Lett. **114**, 191803 (2015). arXiv:1503.07589 [hep-ex]
80. G. Degrassi, S. Heinemeyer, W. Hollik, P. Slavich, G. Weiglein, Eur. Phys. J. C **28**, 133 (2003). arXiv:hep-ph/0212020
81. P. Bechtle, S. Heinemeyer, O. Stål, T. Stefaniak, G. Weiglein, Eur. Phys. J. C **74**(2), 2711 (2014). arXiv:1305.1933 [hep-ph]
82. P. Bechtle, S. Heinemeyer, O. Stål, T. Stefaniak, G. Weiglein, JHEP **1411**, 039 (2014). arXiv:1403.1582 [hep-ph]
83. B.C. Allanach, G. Hiller, D.R.T. Jones, P. Slavich, JHEP **0904**, 088 (2009). doi:10.1088/1126-6708/2009/04/088. arXiv:0902.4880 [hep-ph]
84. S. Chatrchyan et al. [CMS Collaboration], Phys. Rev. Lett. **111**, 101804 (2013). arXiv:1307.5025 [hep-ex]
85. R. Aaij et al. [LHCb Collaboration], Phys. Rev. Lett. **111**, 101805 (2013). arXiv:1307.5024 [hep-ex]
86. V. Khachatryan et al. [CMS and LHCb Collaborations], Nature **522**, 68 (2015). arXiv:1411.4413 [hep-ex]
87. M. Aaboud et al. [ATLAS Collaboration], Eur. Phys. J. C **76**(9), 513 (2016). arXiv:1604.04263 [hep-ex]
88. S. Heinemeyer et al., JHEP **0608**, 052 (2006). arXiv:hep-ph/0604147
89. S. Heinemeyer, W. Hollik, A.M. Weber, G. Weiglein, JHEP **0804**, 039 (2008). arXiv:0710.2972 [hep-ph]
90. S. Heinemeyer, W. Hollik, G. Weiglein, Comput. Phys. Commun. **124**, 76 (2000). arXiv:hep-ph/9812320
91. S. Heinemeyer, W. Hollik, G. Weiglein, Eur. Phys. J. C **9**, 343 (1999). arXiv:hep-ph/9812472
92. M. Frank et al., JHEP **0702**, 047 (2007). arXiv:hep-ph/0611326
93. T. Hahn, S. Heinemeyer, W. Hollik, H. Rzehak, G. Weiglein, Comput. Phys. Commun. **180**, 1426 (2009)
94. T. Hahn, S. Heinemeyer, W. Hollik, H. Rzehak, G. Weiglein, Phys. Rev. Lett. **112**(14), 141801 (2014). arXiv:1312.4937 [hep-ph]. http://www.feynhiggs.de
95. P. Bechtle, O. Brein, S. Heinemeyer, G. Weiglein, K.E. Williams, Comput. Phys. Commun. **181**, 138 (2010). arXiv:0811.4169 [hep-ph]
96. P. Bechtle, O. Brein, S. Heinemeyer, G. Weiglein, K.E. Williams, Comput. Phys. Commun. **182**, 2605 (2011). arXiv:1102.1898 [hep-ph]
97. P. Bechtle et al., Eur. Phys. J. C **74**(3), 2693 (2014). arXiv:1311.0055 [hep-ph]
98. P. Bechtle, S. Heinemeyer, O. Stål, T. Stefaniak, G. Weiglein, Eur. Phys. J. C **75**(9), 421 (2015). arXiv:1507.06706 [hep-ph]
99. V. Khachatryan et al. [CMS Collaboration], JHEP **1410**, 160 (2014). arXiv:1408.3316 [hep-ex]
100. ATLAS Collaboration, ATLAS-CONF-2016–085
101. V. Khachatryan et al. [CMS Collaboration], JHEP **1610**, 006 (2016). arXiv:1603.04053 [hep-ex]
102. V. Khachatryan et al. [CMS Collaboration], Eur. Phys. J. C **74**(9), 3036 (2014). arXiv:1405.7570 [hep-ex]
103. G. Aad et al. [ATLAS Collaboration], JHEP **1405**, 071 (2014). arXiv:1403.5294 [hep-ex]
104. H. Iminniyaz, M. Kakizaki, Nucl. Phys. B **851**, 57 (2011). arXiv:1008.2905 [astro-ph.CO]
105. J.L. Feng, K.T. Matchev, T. Moroi, Phys. Rev. Lett. **84**, 2322 (2000). arXiv:hep-ph/9908309
106. J.L. Feng, K.T. Matchev, T. Moroi, Phys. Rev. D **61**, 075005 (2000). arXiv:hep-ph/9909334
107. J.L. Feng, K.T. Matchev, F. Wilczek, Phys. Lett. B **482**, 388 (2000). arXiv:hep-ph/0004043
108. H. Baer, T. Krupovnickas, S. Profumo, P. Ullio, JHEP **0510**, 020 (2005). arXiv:hep-ph/0507282
109. J.L. Feng, K.T. Matchev, D. Sanford, Phys. Rev. D **85**, 075007 (2012). arXiv:1112.3021 [hep-ph]
110. P. Draper, J. Feng, P. Kant, S. Profumo, D. Sanford, Phys. Rev. D **88**, 015025 (2013). arXiv:1304.1159 [hep-ph]
111. G. Belanger, F. Boudjema, A. Pukhov, A. Semenov, Comput. Phys. Commun. **185**, 960 (2014). arXiv:1305.0237 [hep-ph] (references therein)
112. T. Cohen, M. Lisanti, A. Pierce, T.R. Slatyer, JCAP **1310**, 061 (2013). arXiv:1307.4082
113. J. Fan, M. Reece, JHEP **1310**, 124 (2013). arXiv:1307.4400 [hep-ph]
114. A. Hryczuk, I. Cholis, R. Iengo, M. Tavakoli, P. Ullio, JCAP **1407**, 031 (2014). arXiv:1401.6212 [astro-ph.HE]
115. B. Bhattacherjee, M. Ibe, K. Ichikawa, S. Matsumoto, K. Nishiyama, JHEP **1407**, 080 (2014). arXiv:1405.4914 [hep-ph]
116. M. Baumgart, I.Z. Rothstein, V. Vaidya, JHEP **1504**, 106 (2015). arXiv:1412.8698 [hep-ph]
117. M. Beneke, A. Bharucha, A. Hryczuk, S. Recksiegel, P. Ruiz-Femenia, arXiv:1611.00804 [hep-ph]
118. M. Benito, N. Bernal, N. Bozorgnia, F. Calore, F. Iocco, arXiv:1612.02010 [hep-ph]
119. B.C. Allanach, Comput. Phys. Commun. **143**, 305 (2002). arXiv:hep-ph/0104145
120. G. Isidori, P. Paradisi, Phys. Lett. B **639**, 499 (2006). arXiv:hep-ph/0605012
121. G. Isidori, F. Mescia, P. Paradisi, D. Temes, Phys. Rev. D **75**, 115019 (2007). arXiv:hep-ph/0703035 (references therein)
122. M. Muhlleitner, A. Djouadi, Y. Mambrini, Comput. Phys. Commun. **168**, 46 (2005). arXiv:hep-ph/0311167
123. P. Skands et al., JHEP **0407**, 036 (2004). arXiv:hep-ph/0311123
124. B. Allanach et al., Comput. Phys. Commun. **180**, 8 (2009). arXiv:0801.0045 [hep-ph]
125. F. Mahmoudi, Comput. Phys. Commun. **178**, 745 (2008). arXiv:0710.2067 [hep-ph]
126. F. Mahmoudi, Comput. Phys. Commun. **180**, 1579 (2009). arXiv:0808.3144 [hep-ph]
127. D. Eriksson, F. Mahmoudi, O. Stal, JHEP **0811**, 035 (2008). arXiv:0808.3551 [hep-ph]

128. A. Crivellin, J. Rosiek, P.H. Chankowski, A. Dedes, S. Jaeger, P. Tanedo, Comput. Phys. Commun. **184**, 1004 (2013). arXiv:1203.5023 [hep-ph]
129. J.D. Hunter, Comput. Sci. Eng. **9**(3), 90–95 (2007)
130. A. Buckley, Eur. Phys. J. C **75**(10), 467 (2015). arXiv:1305.4194 [hep-ph]
131. F. Feroz, M.P. Hobson, Mon. Not. R. Astron. Soc. **384**, 449 (2008). arXiv:0704.3704 [astro-ph]
132. F. Feroz, M.P. Hobson, M. Bridges, Mon. Not. R. Astron. Soc. **398**, 1601–1614 (2009). arXiv:0809.3437 [astro-ph]
133. F. Feroz, M.P. Hobson, E. Cameron, A.N. Pettitt, arXiv:1306.2144 [astro-ph]
134. G. Aad et al. [ATLAS Collaboration], Phys. Rev. D **88**(11), 112006 (2013). arXiv:1310.3675 [hep-ex]
135. G. Salam, A. Weiler, http://collider-reach.web.cern.ch/collider-reach
136. M. Low, L.T. Wang, JHEP **1408**, 161 (2014). arXiv:1404.0682 [hep-ph]
137. S.A.R. Ellis, B. Zheng, Phys. Rev. D **92**(7), 075034 (2015). arXiv:1506.02644 [hep-ph]
138. G. Aad et al. [ATLAS Collaboration], JHEP **1409**, 176 (2014). arXiv:1405.7875 [hep-ex]
139. The ATLAS collaboration [ATLAS Collaboration], ATLAS-CONF-2016-078
140. The ATLAS collaboration [ATLAS Collaboration], ATL-PHYS-PUB-2012-001
141. The ATLAS collaboration [ATLAS Collaboration], ATL-PHYS-PUB-2014-010
142. T. Cohen, T. Golling, M. Hance, A. Henrichs, K. Howe, J. Loyal, S. Padhi, J.G. Wacker, JHEP **1404**, 117 (2014). arXiv:1311.6480 [hep-ph]
143. CMS Collaboration [CMS Collaboration], CMS-PAS-SUS-16-024
144. B.S. Acharya, K. Bozek, C. Pongkitivanichkul, K. Sakurai, JHEP **1502**, 181 (2015). arXiv:1410.1532 [hep-ph]
145. S. Jung, JHEP **1406**, 111 (2014). arXiv:1404.2691 [hep-ph]
146. S. Gori, S. Jung, L.T. Wang, J.D. Wells, JHEP **1412**, 108 (2014). arXiv:1410.6287 [hep-ph]
147. C. Cheung, L.J. Hall, D. Pinner, J.T. Ruderman, JHEP **1305**, 100 (2013). arXiv:1211.4873 [hep-ph]
148. H. Baer, V. Barger, D. Mickelson, Phys. Lett. B **726**, 330 (2013). arXiv:1303.3816 [hep-ph]
149. D. Barducci, A. Belyaev, A.K.M. Bharucha, W. Porod, V. Sanz, JHEP **1507**, 066 (2015). arXiv:1504.02472 [hep-ph]
150. M. Badziak, A. Delgado, M. Olechowski, S. Pokorski, K. Sakurai, JHEP **1511**, 053 (2015). arXiv:1506.07177 [hep-ph]
151. A. Tan et al. [PandaX-II Collaboration], Phys. Rev. Lett. **117**(12), 121303 (2016). arXiv:1607.07400 [hep-ex]
152. D.S. Akerib et al., arXiv:1608.07648 [astro-ph.CO]
153. D.C. Malling, D.S. Akerib, H.M. Araujo, X. Bai, S. Bedikian, E. Bernard, A. Bernstein, A. Bradley et al., arXiv:1110.0103 [astro-ph.IM]
154. E. Aprile et al. [XENON Collaboration], JCAP **1604**(04), 027 (2016). arXiv:1512.07501 [physics.ins-det]
155. E. Aprile et al., https://idm2016.shef.ac.uk/indico/event/0/session/5/contribution/76/material/slides/0.pdf
156. P. Cushman, C. Galbiati, D.N. McKinsey, H. Robertson, T.M.P. Tait, D. Bauer, A. Borgland, B. Cabrera et al., arXiv:1310.8327 [hep-ex]
157. J. Gasser, H. Leutwyler, M.E. Sainio, Phys. Lett. B **253**, 252 (1991)
158. M. Knecht, arxiv:hep-ph/9912443
159. M.E. Sainio, PiN Newslett. **16**, 138 (2002). arXiv:hep-ph/0110413
160. L. Baudis, DARWIN Consortium Collaboration. J. Phys. Conf. Ser. **375**, 012028 (2012). arXiv:1201.2402 [astro-ph.IM]
161. J.R. Ellis, A. Ferstl, K.A. Olive, Phys. Lett. B **481**, 304 (2000). arXiv:hep-ph/0001005 (For some discussions of these cancellations)
162. V. Mandic, A. Pierce, P. Gondolo, H. Murayama, arXiv:hep-ph/0008022
163. J.R. Ellis, J.L. Feng, A. Ferstl, K.T. Matchev, K.A. Olive, Eur. Phys. J. C **24**, 311 (2002). arXiv:astro-ph/0110225
164. P. Huang, C.E.M. Wagner, Phys. Rev. D **90**(1), 015018 (2014). arXiv:1404.0392 [hep-ph]
165. T. Han, F. Kling, S. Su, Y. Wu, arXiv:1612.02387 [hep-ph]
166. E. Bagnaschi et al., Likelihood Analysis of the pMSSM11 in Light of LHC 13-TeV Data. preprint [CERN-TH-2017-087], [DESY 17-059], [IFT-UAM/CSIC-17-035], [KCL-PH-TH/2017-22]